Experimental examination of growing and newly submerged sea ice including acoustic probing of the skeletal layer

K.L. Williams, G.R. Garrison, and P.D. Mourad

Applied Physics Laboratory, College of Ocean and Fishery Sciences, University of Washington, Seattle, Washington 98105

(Received

Results of an in-situ experiment to examine acoustic parameters and scattering properties of growing and newly submerged arctic sea ice are presented. The primary emphasis is on the acoustic properties of highly porous sea ice. High resolution (to about 1 cm) vertical profiles of the longitudinal wave speed in growing and submerged sea ice are derived from the experimental data. The results indicate a skeletal layer about 3 cm thick at the bottom of the growing ice. The time dependence of vertical sound speed profiles in a submerged ice block reveals a long time scale process of up to 80 hours and a short process of a few hours. The former process is the warming of the block; the later is thought to be due to the disturbance of hydrostatic equilibrium as the ice is submerged. Concurrently with the wave speed measurements, scattering from the undersurface of the ice was measured at several frequencies. A comparison with predictions based on the sound speed data demonstrates the ability to predict normal incidence ice reflectivity from sound speed profiles as well as the viability of using scattering data in inversions to obtain sound speed profiles. Absorption of a longitudinal wave propagating vertically in ice was also measured. The peak absorption rate found in the skeletal layer was between 2 and 5 dB/cm at 92 kHz. The temperature dependence of absorption seen in the submerged ice suggests that the McCammon-McDaniel equation ($\sim T^{-2/3}$) is useful away from the skeletal layer. The measurements of ice temperature as a function of time and depth allow a calculation of the thermal diffusivity of the upper region of

92 8 3 0248

growing sea ice (0.0080 cm^2/s) and an "effective" thermal diffusivity of the sub-

merged ice block (about 0.0015 cm^2/s). Measurements of salinity profiles in the ice,

along with the temperature profiles, are used to calculate porosity, which is then

used in models of the longitudinal wave speed as a function of porosity. A compar-

ison between models and experiment is employed in suggesting a possible mecha-

nism for the increased speed seen experimentally in the bottom portion of the ice

after submergence.

PACS numbers: 43.20.Fn, 43.30.Ma, 43.30.Pa

INTRODUCTION

The acoustic properties of sea ice are inherently important to studies of sound propagation and

scattering in the Arctic.[1-4] The richness of the acoustic behavior of sea ice stems from its saline

nature. In particular, sea ice is the result of the solidification of a sub-eutectic melt.[5,6] This accounts

for the high porosity layer at the ice/water interface, known as the "skeletal" layer. The high po-

rosity makes measurements of the acoustic properties in the skeletal layer extremely sensitive to

perturbations. Because this layer is a few centimeters thick, it is of primary importance for model-

ing the scattering of high frequency (above 10 kHz) acoustic energy from the underside of the ice.

The porosity of sea ice is controlled by its salinity and temperature. [7] For a constant salinity,

an increase in temperature is accompanied by an increase in porosity. Thus if a block of sea ice is

submerged, and thereby warmed during keel formation, the entire block may become highly po-

rous. In this case the dimensions of the block, or of a structure made from many blocks, are the

appropriate length scales to use in determining the frequency range where the acoustic behavior of

high porosity ice is important. Since the ice blocks that form keels in the Arctic have length scales

on the order of meters and the keels have scales on the order of tens of meters, that frequency range

extends below 100 Hz.

Because high porosity sea ice is sensitive to disturbance, we measured its acoustic properties

in situ. We also measured salinity and temperature, not only for information about the physical pa-

rameters of the ice (e.g., porosity and thermal diffusivity), but to relate these properties to the mea-

sured acoustical properties (longitudinal wave sound speed, reflectivity, and absorption). The experimental apparatus and method have produced high vertical resolution measurements (to about 1 cm) of acoustic properties in high porosity sea ice both during growth and after submergence.

The article is organized as follows. Section I describes the experimental instrumentation, arrangement, and procedure, as well as some of the environmental conditions during the experiment. Section II gives the main results, dealing first with growing ice and then with submerged ice. Section III is a summary of results. The appendix details the calculations for obtaining the thermal diffusivities quoted in the body of the paper.

I. EXPERIMENT

The experiment was conducted at an Applied Physics Laboratory Ice Station (APLIS) established in the Beaufort Sea and occupied from the end of February to the middle of April 1990. In the first part of the experiment, a 2-m square hole was cored in the ice and sensor arrays were suspended in the water to monitor conditions as ice formed around them. The ice grew to about 42 cm thickness in 10 days. During this time, the temperature and salinity of the growing ice were monitored while measurements were made of the vertical longitudinal wave speed and attenuation. The normal incidence acoustic reflectivity of the growing sea ice was also measured from a transducer below at frequencies from 40 to 220 kHz.

In the next phase of the experiment, an ice block was cored from a portion of the newly grown ice containing the sensors. This block, a cylinder about 58 cm in diameter and 42 cm in height, was submerged and held in place while we made periodic measurements of temperature, longitudinal wave sound speed, attenuation, and reflectivity (similar to those taken in the first part of the experiment) until the ice reached thermal equilibrium with the surrounding water (about 80 hours).

Details of the experiment are given in the following subsections. Section I.A discusses the sensor arrays and the transmitter/receiver acoustic transducers. Section I.B outlines the experiment arrangement and procedure. Section I.C describes some general environmental conditions.

DTIC QUALITY INSPECTED 3

A-1

Revised 10 June

A. Instrumentation

The in-water instrumentation comprised two vertical thermistor arrays, a vertical hydrophone array, and two transmitter/receiver acoustic transducers. The on-ice instrumentation consisted of switching boxes for selecting particular sensors in the vertical arrays. All electronics control, signal generating, and data recording instrumentation were housed in a plywood building about 50 m from the experiment site.

The two transmitter/receiver units were a "platter" and a "sonar" transducer. The platter[8] was used for the normal incidence reflectivity measurements and to measure ice growth. An independent measure of ice growth was made with the sonar[9] transducer.

The thermistor and hydrophone arrays were built in-house. Two thermistor arrays were constructed using Yellow Springs Instrument (YSI) precision thermistors with impedance-to-temperature calibrations matched to 0.2°C. Each thermistor was encased in marine epoxy. The hydrophone array was made of PZT ceramic elements approximately cubic in shape (0.5 cm per side) with a resonance frequency around 200 kHz. Each element was placed at the end of a small Plexiglas tube (0.5 cm o.d. and 5 cm in length) and encased in PRC (Products Research and Chemical Company) potting compound. The arrays were constructed using Plexiglas tubing (o.d. 1.5 - 2 cm and length about 90 cm) and marine epoxy. The wire leads running from arrays to switching boxes were enclosed in surgical tubing. Each thermistor array contained 24 sensors spaced approximately 2 cm apart. The hydrophone array had 12 sensors, the upper half spaced about 5 cm apart and the lower half about 2.5 cm apart. The total vertical coverage of the arrays (45 cm) was based on predicted freezing rates and the time allotted for the experiment (two weeks).

Figure 1 shows two of the vertical arrays (hydrophones to the left). Note that the hydrophones were arranged in a helix to prevent acoustical shadowing. Figure 2 gives the vertical spacings of these sensors and the horizontal spacing between the thermistor and hydrophone arrays.

Switching boxes on the ice were connected to Nim-Bin control modules built in-house. The hy-   NIM-l
drophone control module allowed access to any 2 of the 12 hydrophones. The thermistor control module accessed any sensor in the thermistor arrays. Waveform generation, amplification, and re-
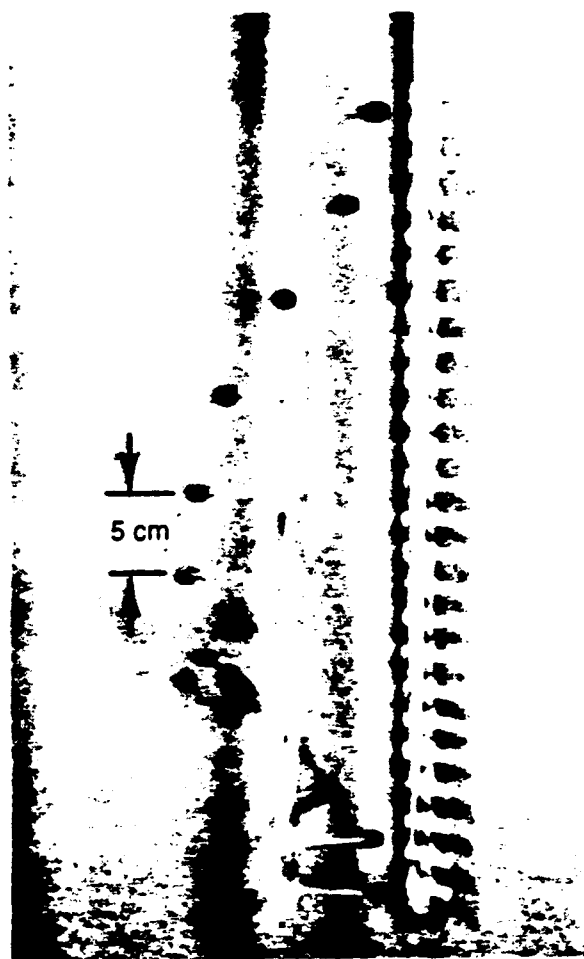
FIG. 1. Array of hydrophones (at left) and thermistors (at right) that were suspended in the center of a 2-m square hole in the ice. Both arrays were suspended from a wood 2x4 across the hole.
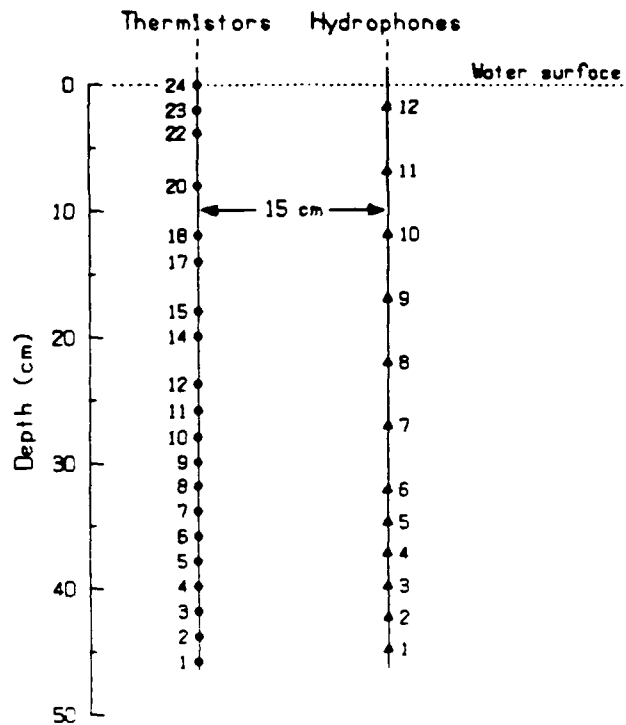
FIG. 2. Depths of the suspended hydrophones and thermistors. The top thermistor, #24, was at the ice/air interface. Inoperable sensors (e.g., #13) have been omitted.

ception for the platter transducer were performed by the APL MAME[10] system. The sonar transducer had its own control box. All acoustic signals were recorded on a Nicolet digitizing scope. The resistances measured for each thermistor were recorded by hand.

B. Experimental Arrangement and Procedure

The ice canopy was about 2 m thick at the experiment site. Two 2-m square holes were cut through the ice canopy, one for the main experiment and the other for monitoring. The later was 3 m, center to center, from the main hole. One of the thermistor arrays and the hydrophone array were vertically supported at the center of the main hole. The other thermistor array was suspended at the center of the monitor hole. Each thermistor array was arranged so that the top sensor was at the water/air interface. Figure 3 is a diagram of the in-water instrumentation in the main hole during the submergence phase, discussed later.

Salinity measurements were taken on sections of ice cores from the monitor hole during the ice growth phase. Cores were taken from this hole to avoid disturbing the main hole from which an ice block was to be cored for the second part of the experiment.The second thermistor array let us determine whether ice samples in the two holes were in equivalent states. The effort to obtain cores was worthwhile, considering the importance of salinity in determining ice properties (e.g., porosity). However, the invasive nature of the technique causes the salinity measurements to be of lower resolution and quality than the temperature and acoustic parameter measurements.

The platter transducer shown in Fig. 3 was suspended from three lines 120° apart, which were easily adjusted to place the transducer directly below the hydrophone array.[8] The "sonar" transducer was on a rotating arm so that it could be placed below the arrays during the ice growth phase and then moved away before the ice block was submerged. The short acoustic pulses emitted from these transducers were reflected from the ice/ water interface and then received back at the transducers. They were used to determine ice thickness as a function of time, as well as the reflectivity of the ice as a function of frequency. The platter transducer's emissions were received by the hydrophone array, allowing measurement of ice acoustic parameters.

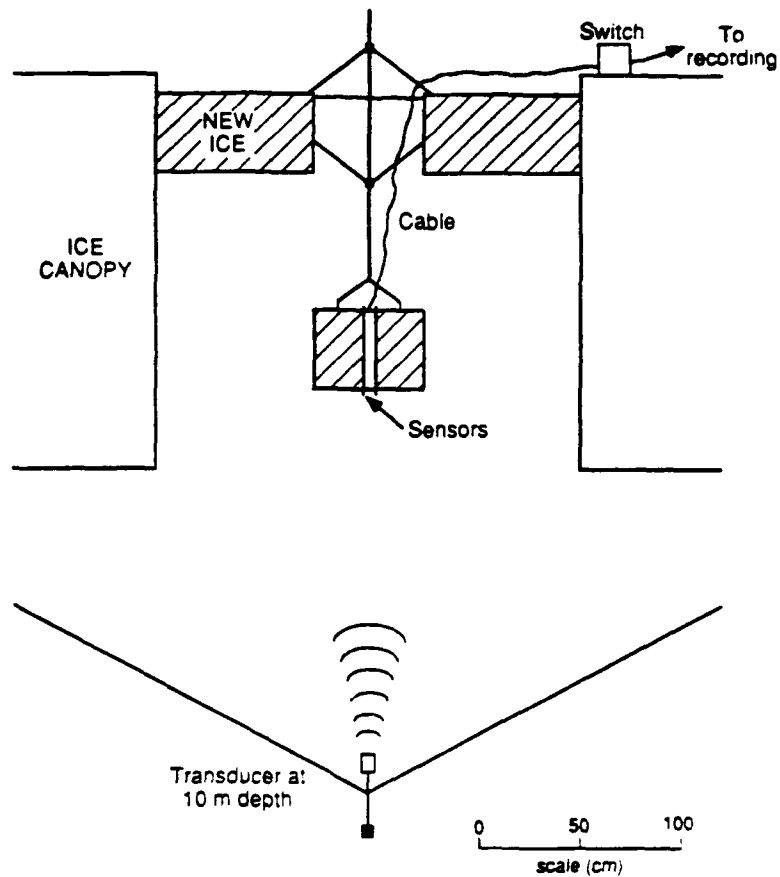Measurements for determining reflectivities, acoustic parameters, and temperature of the ice

FIG. 3. Arrangement after the ice in the 2-m hole had grown to 42 cm and a block of this new ice had been cored and submerged. (Depth of transducer not to scale.)

were made several times each day during the ice growth phase of the experiment. After submergence of the ice block, the same type of measurements were made, but more frequently (30 measurements in the 80 hours monitored after submergence). The results derived from these measurements and the salinity measurements form the bulk of Sec. II.

C. Environmental Conditions

A portable weather station was operated at APLIS to record air temperature, wind speed, etc. Figure 4 shows a curve of the air temperature recorded, along with the temperatures determined from the top sensors in the two thermistor arrays during the ice growth phase. The array temperatures tended to be higher than the weather station temperatures. This could be due to snow coverage when winds cause drifting. The holes were cleared of snow periodically, but not always immediately before measurement. Note, however, that the two thermistors are always in close agreement, which indicates that the ice freezing process was being driven by the same thermal gradient at the two holes. Note too that in the last day of the ice growth phase a significant front moved in, with air temperature increasing more than 10°. This rapid rise allowed a calculation of thermal diffusivity using the vertical profiles of the temperature of the ice during that time.

In Fig. 5 the salinity and temperature profiles measured from ice cores extracted from the 42-cm ice in the monitor hole on the last day of the ice growth phase are compared with profiles for a region of the ice canopy near the experiment. Data for the deepest few centimeters of high porosity ice are not included because brine drainage during extraction typically makes them unreliable. The computed porosity and the longitudinal wave sound speed derived[11] using this porosity are also shown in this figure. The low salinity region near the top of the canopy profile, and the overall low salinity, indicate that the ice in this region has gone through at least one warming period and is thus probably multiyear ice. In Sec. II.4, speeds predicted from Ref. 11 will be compared with those experimentally determined in the present effort.
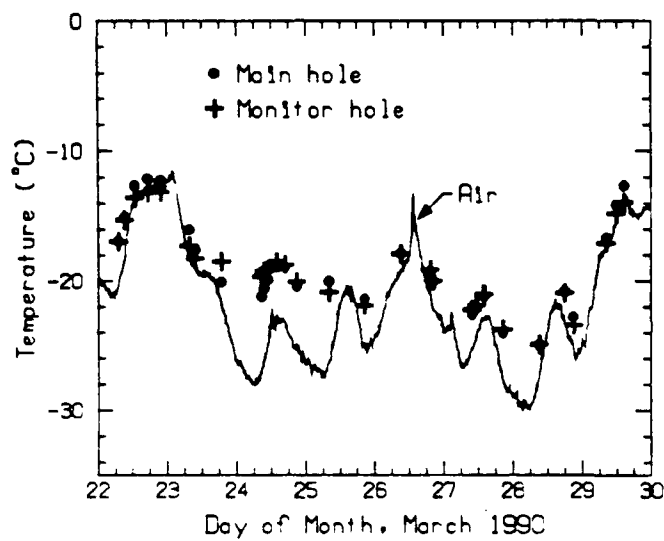
6

FIG. 4. A comparison of air temperatures from the camp weather station with temperatures record-ed by thermistors located at the ice/air interface. Array temperatures tend to be higher than weather station temperatures, probably owing to snow cover.
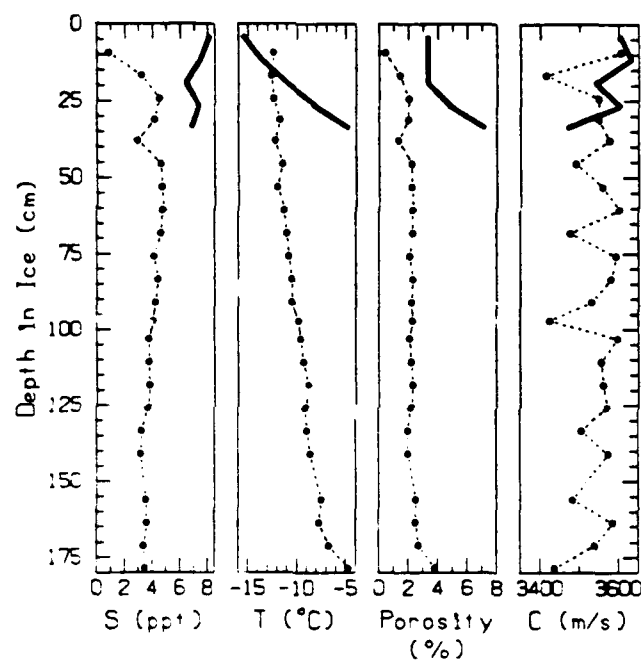
FIG. 5. Measured temperature and salinity of ice cores taken from the canopy in the vicinity of the ice growth experiment (dashed lines). The porosity and sound speed profiles are calculated. The solid lines are a similar presentation for data obtained from cores taken on the last day of the ice growth experiment.

II. RESULTS

A. During Ice Growth

1. Freezing rate

At the beginning of the experiment, with the platter transducer suspended beneath the 2-m hole, we measured acoustic reflections from the surface of the hole after the water surface was swept clear of ice crystals. Measurements were taken at several frequencies: 37, 52, 92, 150, and 220 kHz. Reflections arriving before the surface reflection were identified as either the bottom of the ice canopy, the arm that supported the sonar transducer, or the lower end of the sensor strings. These fixed references were necessary because the platter's depth varied as the supporting lines stretched.

For the first part of the reflection measurements, ice growth was determined by comparing the reflection time for the ice with the reflection time for one of the sensor strings at 220 kHz. Later, the rotating arm reflection fell within the digitizing window and the ice reflection time was then compared with the arm reflection time at 92 kHz. In determining ice growth, we used a sound velocity C_w for water of 1436 m/s, calculated using CTDs taken nearby. Increase in ice depth for the growth period is shown in Fig. 6.

Also shown are the results of an independent measure of ice growth using the sonar transducer, which operated at 92 kHz with short (0.5 ms) cw pulses. The ice reflection return for this transducer was recorded on a digital oscilloscope about twice per day. To obtain the ice depth, we compared the return times with those from the air/water interface at the start of the experiment.

A curve has been drawn in Fig. 6 to best represent both sets of data. It gives the distance from initial water surface to the lower surface of the ice, to an accuracy of about 0.5 cm.

2. Temperature monitoring and calculation of thermal diffusivity

Readings of the thermistor string were taken three to six times per day during the ice growth phase of the experiment. The measured resistances were converted to temperature with a calibration curve, supplied by YSI and confirmed when the string was prepared in the laboratory.

A plot of temperature vs time for each thermistor is shown in Fig. 7. The thermistors near the surface follow the air temperature (Fig. 4). The air temperature variations appear to penetrate about
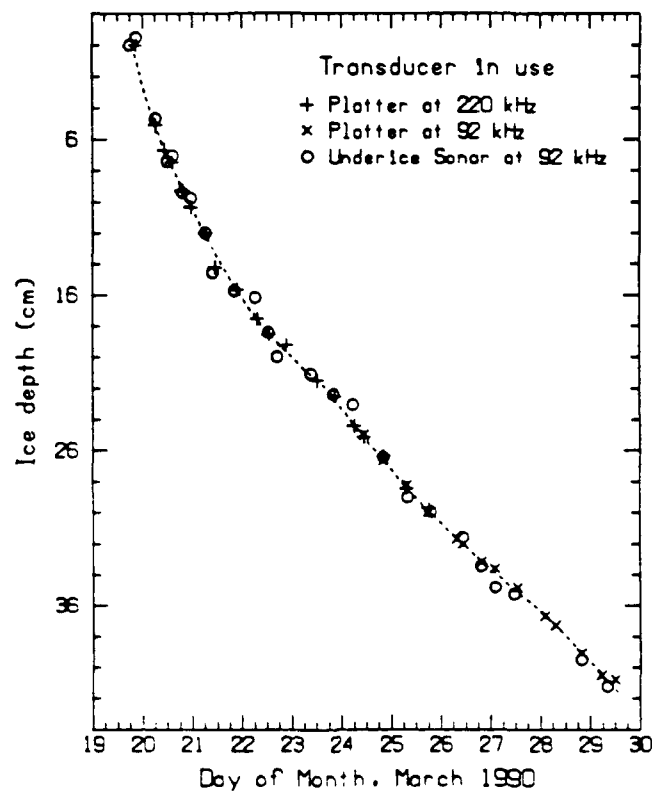
7

FIG. 6. Ice depth during the ice growth phase as determined acoustically from two different trans-ducers suspended below the hole. Initially, the water surface was the reference for returns to the platter transducer; later, because the platter depth varied, the reflections from the bottom of the sensor array and the arm for the sonar transducer were used.
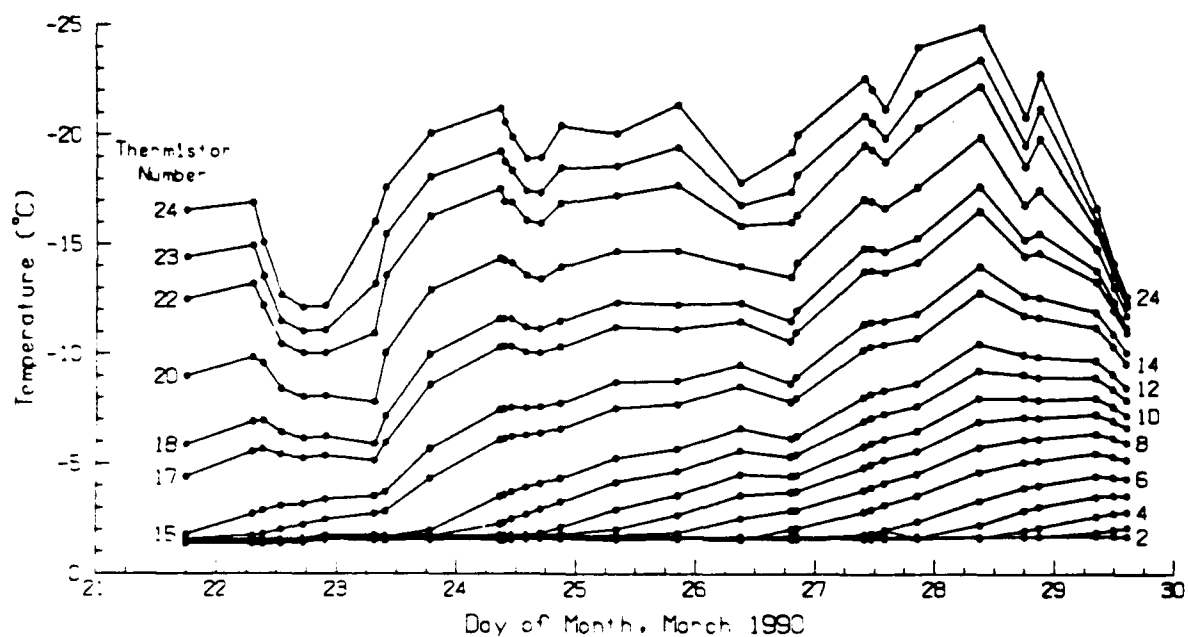
FIG. 7. The temperatures recorded at each thermistor during ice growth. The temperature scale has been inverted from that for the air temperatures in Fig. 4 so that the graphs could be nested.

20 cm into the ice, to thermistor 14, with a lag due to diffusivity. Temperature profiles for the same data are plotted in Fig. 8. The first profile at the right (No. 1) shows a water temperature for all thermistors below 18 cm, and a colder temperature for all above 18 cm, indicating that the ice had frozen to that depth before temperature readings began. (There was a delay in temperature monitoring because of hardware problems in the thermistor NIM-bin module.) With time, most of the temperatures decreased except for changes related to air temperature variations. On 29 March when the air temperature rose to -14°C, the upper 30 cm of the profiles shifted as shown by the four dotted lines in Fig. 8. The coldest profile (No. 25) was for 0915 on 28 March, the time of the coldest air temperature (Fig. 4).

We used the change in the ice temperature profile on 29 March to calculate thermal diffusivity assuming a constant diffusivity in the upper region of the ice (the portion below -6°C). The calculation (detailed in the appendix) indicates a thermal diffusivity of about 0.0080 cm²/s. In reality, the diffusivity is a function of salinity and temperature, with the most severe temperature dependence for values above -6° C. This becomes evident in the calculation for thermal diffusivity carried out for the submerged ice block (Sec. II.B). Reference 12 gives approximate equations for the salinity and temperature dependence of thermal diffusivity for temperatures above -8°C. These equations predict a thermal diffusivity of 0.0054 cm²/s at -8°C (also shown in the appendix). The upper limit of the diffusivity can be set using the nonsaline ice value of about 0.012 cm²/s at -20° C. These results are consistent with the value given above.

3. Sound speed monitoring and initial estimate of skeletal zone thickness

Travel times between hydrophones were measured when the array was first placed in the water. These times, along with the known sound speed in the water (C_w), give the separations between the acoustic centers of the hydrophones. We calculated the average sound speed between any two hydrophones at various times after they were frozen in by dividing the spacing by the travel time. Although we did not have enough electronics to receive each ping at all hydrophones, we were able to receive at two adjacent hydrophones for the same ping. By progressing through the array, we obtained data that were not affected by ping-to-ping variations in the transmitter output.
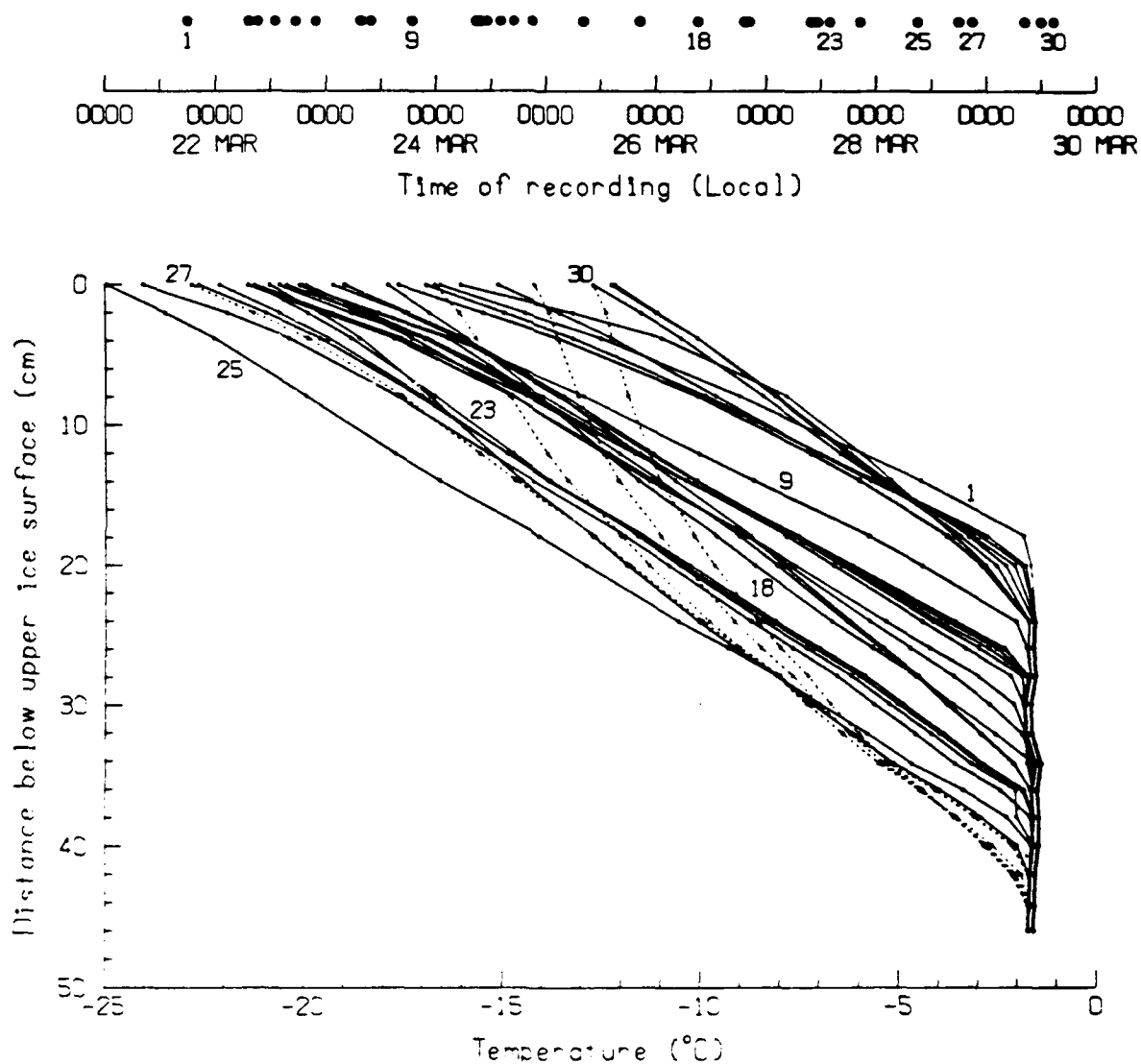
FIG. 8. Temperature profiles for the data of Fig. 7. Several profiles are labeled by run number; the graph at the top of the figure associates run number with local time. The dotted lines show the effect of a 12°C rise in ambient temperature on 29 March

There were two major difficulties with the experimental data. First, hydrophone 10 had a very low signal to noise ratio (SNR) compared with the other hydrophones, making the in-water calibration timing measurement difficult. During much of the experiment the SNR problem was compensated for by using the Nicolet's averaging capabilities. The second difficulty was that some ice had formed to a depth below hydrophone 11 before the "in-water" measurements of travel times were made. However, good estimates of the separation between acoustic centers for hydrophones 10-12 were obtained by comparing all calibration times with rule-measured spacings.

The sound speed in each hydrophone interval is plotted in Fig. 9 as a function of time. As the ice froze in each interval the sound speed rose above C_w. After the speed reached about 3500 m/s, it varied (presumably) because of changes in air temperature which penetrated the ice and changed its porosity.

Figures 6 and 9 can be used to make an initial estimate of the thickness of the "acoustic" skeletal layer, which we here define as the thickness of the layer between the ice/water interface and the point where the vertical speed reaches 3500 m/s. We chose this definition because variations in speed due to changes in atmospheric conditions are apparent at higher speeds (Fig. 9).

Consider the curve in Fig. 9 for hydrophone interval 8–9 (labeled 8). If we approximate this curve as a straight line, it increases from C_w to 3500 m/s in about 44 hours. In Fig. 6 the slope of the curve between 16.9 and 22.0 cm (the depths of hydrophones 8 and 9) gives a freezing rate of 0.15 - 0.16 cm/h. The speed starts deviating from C_w as ice begins to form in the interval between hydrophones. For an initial estimate, we assume that the skeletal layer has completely traversed the interval when the speed reaches 3500 m/s. With this assumption and the spacing between hydrophones from Fig. 2, curve 8 gives a skeletal layer thickness of 1.5 to 1.9 cm. Similarly, curve 5 gives a thickness of 2.7 to 3.1 cm. These are clearly underestimates of the layer thickness since the lower hydrophone in an interval would still be in the skeletal zone when the average speed in the interval reaches 3500 m/s. Furthermore, the underestimate is more severe for curve 8 since the interval between hydrophones 8 and 9 is about twice that between hydrophones 5 and 6. The next subsection uses the entire data set to obtain both a better estimate of the skeletal layer thickness and
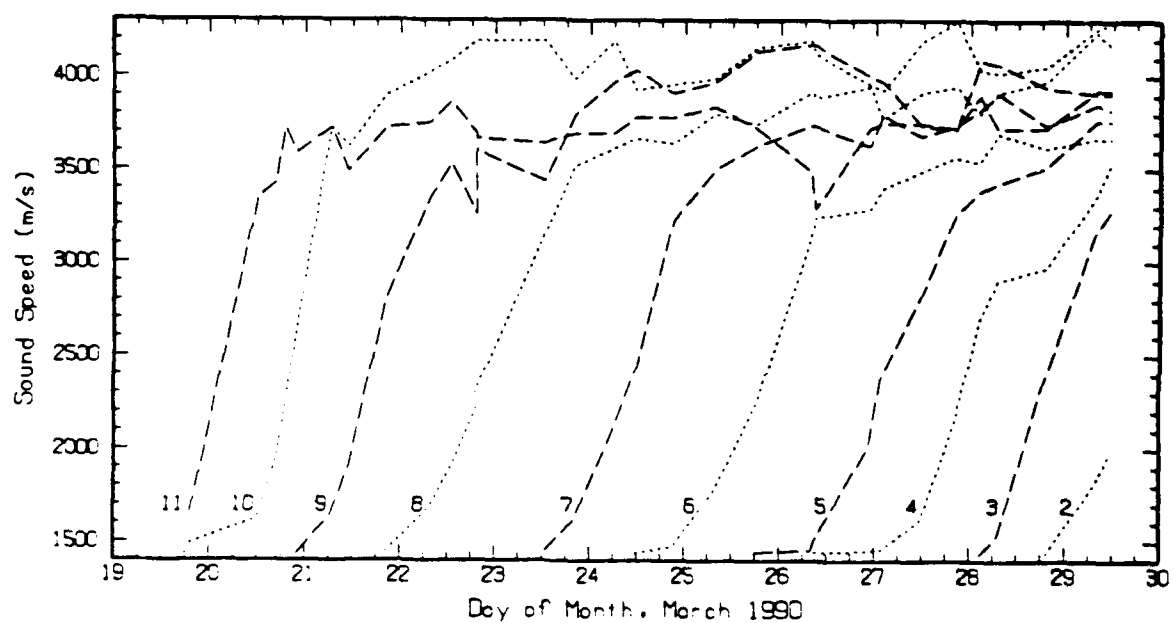
9

FIG. 9. The change in sound speed as measured for each hydrophone pair as the ice formed, covering one hydrophone after another. The number of the deeper of the pair is given.

an estimate of the velocity profile within the skeletal layer.

4. Sound speed in the skeletal layer

Every set of sound speed measurements included a measurement across the lowest few centimeters of ice. We assumed the skeletal layer formed consistently at all depths, and combined all data to obtain a sound speed profile for the layer.

The sound speed $C_I(s)$ in ice as a function of distance (s) away from the ice/water interface was determined by first considering hydrophone intervals that included the interface (Fig. 10a). To determine the extent of the ice below a hydrophone, the depth of the interface at the measurement time was taken from Fig. 6. An average value for the acoustic speed $\bar{C}_I(s)$ in this portion of ice was then calculated using C_w and the average speed C_a in the interval between the adjacent hydrophones. To get larger values of s, the interval was extended to other hydrophones above (Fig. 10b); the average speed was determined by adding travel times for intervals up to 15 cm. These are plotted as points in Fig. 10c. These were fitted with a fourth order polynomial (dotted line in Fig. 10c) giving, for s in centimeters,

$$\bar{C}_I(s) = 1490 + 480.93s - 55.670s^2 + 3.2548s^3 - 0.071579s^4. \tag{1}$$

which is a good fit for an s of 0 to 15 cm. The total travel time through the ice can be expressed as either an integral or in terms of the average speed given in Eq. (1). Taking the derivative of this travel time equality with respect to s gives

$$\frac{d}{ds}\left(\int_0^s \frac{dx}{C_I(x)} \right) = \frac{d}{ds}\left(\frac{s}{C_I(s)} \right) \tag{2}$$

10

or

$$C_I(s) = \frac{\overline{C}_I^2(s)}{(\overline{C}_I(s) - s\frac{d}{ds}\overline{C}_I(s))}, \tag{3}$$

which is the result plotted as a solid line in Fig. 10c. It is shown only to $s=7$ cm; beyond this point it becomes erratic because we have only sparse data for the large s values in the fourth order fit of Eq. (1).

To obtain sound speeds farther into the ice, average speeds for some hydrophone pairs were determined in intervals where the speed had reached a plateau. The values obtained are plotted as open circles in Fig. 10c and extend the speed profile beyond the end of the solid line. *The result is a high resolution, in-situ, vertical profile for the speed of the longitudinal wave in growing arctic sea ice.*

The "acoustic" skeletal layer thickness apparent from the solid line is about 3 cm. As expected, this is larger than our initial estimates discussed earlier. We use the term "acoustic" skeletal layer because the thickness measured here may differ from that obtained by examining the ice structure directly. However, the value found is commensurate with those reported in Ref. 13 (3 cm) and Ref. 14 (1.8 to 5.75 cm).

5. Absorption of sound

The hydrophone data were also used to calculate the absorption of sound in the ice at different temperatures. Recording each ping on two adjacent hydrophones simultaneously allowed a comparison of amplitudes with no effects from ping-to-ping variability in the transmitter. The relative sensitivities of the hydrophones in water were obtained by recording signals before any ice had formed. We calculated the absorption of sound in the ice assuming that the sensitivity of a hydrophone did not decrease when ice formed around it. If both hydrophones were in ice, both sensitivities would change about the same, and our calculated absorption would be accurate. However, if only the upper hydrophone was in ice and its sensitivity did indeed decrease, our calculated absorption for the bracketed ice, which generally includes the skeletal layer, would be high.
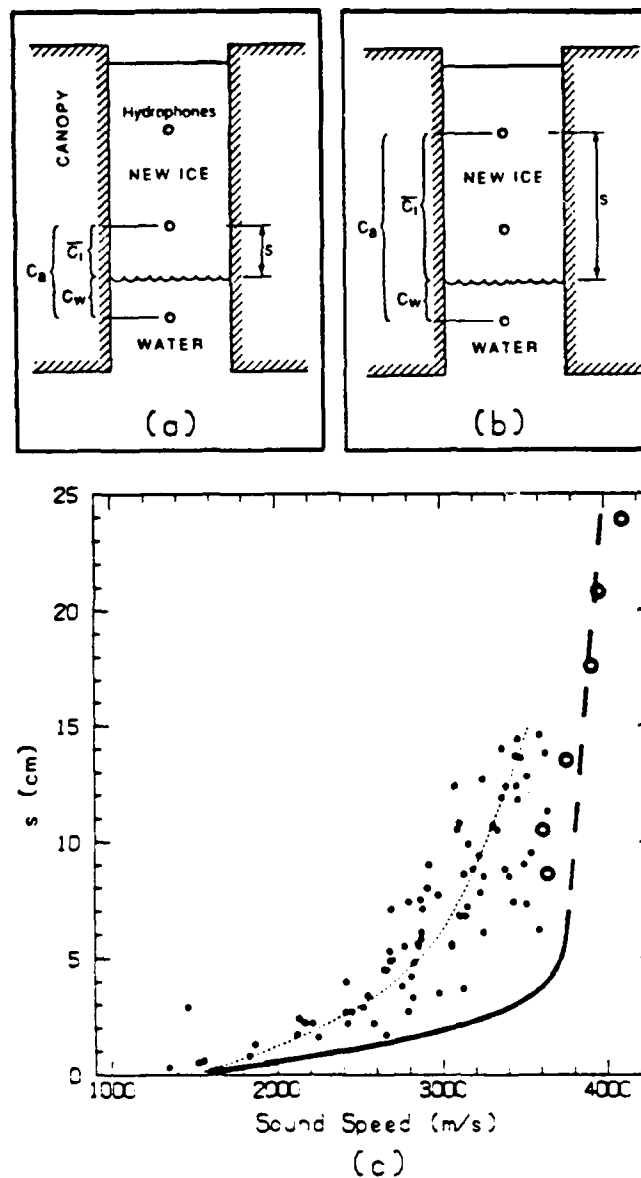
FIG. 10. The average sound speed for a distance s into the ice is calculated using the measured travel times between a hydrophone just below the ice surface and one just above as in (a). To obtain larger s values. the second or third hydrophone above the ice surface was substituted for the upper one. as in (b). This gives two or three values of average sound speed versus s for every set of measurements during the ice growth experiment. these are plotted as dots in (c). From a least squares fit of these data. Eq. (1). the profile in the ice has been calculated. Eq (3). and shown as a solid line. The line is extended to fit some sound speed measurements (circles) obtained from hydrophone pairs well into the ice.

For adjacent hydrophones a distance (s) centimeters apart with amplitude readings of A' and B' in water, and A and B after partial or complete embedment, the absorption loss (in decibels) is calculated as

$$L_t = 20\log\left(\frac{AB'}{BA'}\right).\qquad(4)$$

This total absorption loss can be expressed in terms of an interface loss p and an absorption coefficient per centimeter α as

$$L_t = p + \int_0^s \alpha(s)\,ds\qquad(5)$$

If we use the temperature dependence of the McCammon-McDaniel equation[3] for the absorption coefficient, i.e.,

$$\alpha = kf\left(-\frac{6}{T}\right)^{2/3}\qquad(6)$$

(where T is temperature in degrees Celsius, k is a constant, and f is frequency in kilohertz) and assume a linear temperature profile in the ice, Eq. (5) can be written as an integral over temperature to obtain

$$L_t = p + kfqs,\qquad(7)$$

where q is the integrated temperature effect for thickness s. With temperature T_2 at the upper hydrophone and T_1 at the lower hydrophone,

$$q = 3(6^{2/3})\left(\frac{(-T_2)^{1/3} - (-T_1)^{1/3}}{(T_1 - T_2)}\right)\qquad(8)$$

Revised 10 June

In Eq. (6) intergrain friction is assumed to be the cause of the acoustic absorption. Again, this is most probable away from the skeletal layer. Within the layer, relative fluid/solid motion (as accounted for in the Biot model of a porous medium) may dominate[15] over frame loss, such as intergrain friction, giving large attenuations with a different frequency dependence than in Eq. (6). Equation (7) shows that a plot of measured loss vs fqs should display a linear variation with slope k. If temperatures along the path are measured, q can be determined more accurately by numerically integrating over each hydrophone interval.

Pairs of amplitude readings were taken for each interval before any ice appeared in the interval. Their ratios were fairly consistent, showing that the equipment was capable of repeatable loss measurements. Averages of these ratios over several measurements provide a calibration of the receiving circuits.

We now examine the absorption loss as the freezing progressed. Data for hydrophones 10-12 are unusab.e, as mentioned earlier. Proceeding downward, losses were measured for all hydrophone intervals in which ice was present. Figure 11 shows how the loss for travel from hydrophone 7 to 8 and 8 to 9 varied throughout the several runs. A plot of the sound speed is shown for comparison. The high absorption appears to occur where the sound speed is increasing, i.e., within the skeletal layer. (As a point of reference, measurements[16] we have made by other techniques indicated a total absorption in the skeletal layer of about 2.3 dB.)

Absorption in the skeletal layer can be examined using the entire data set. In every set of measurements the lower surface of the ice lies between two hydrophones. Thus, in this hydrophone interval there is both ice and water. The temperature at the hydrophone above the ice interface is interpolated, assuming a constant gradient between thermistors. This and the water temperature are used to compute q for the layer. The transmission loss between the hydrophones is assumed to occur in the ice, of thickness s. When the loss is computed for many measurements, and thus many values of s, we have a relationship showing the loss in various thicknesses of the skeletal layer. Some additional data points were obtained by taking an interval involving two hydrophones, summing the two losses, and thus obtaining some larger values for s. All data are plotted in Fig. 12.

13
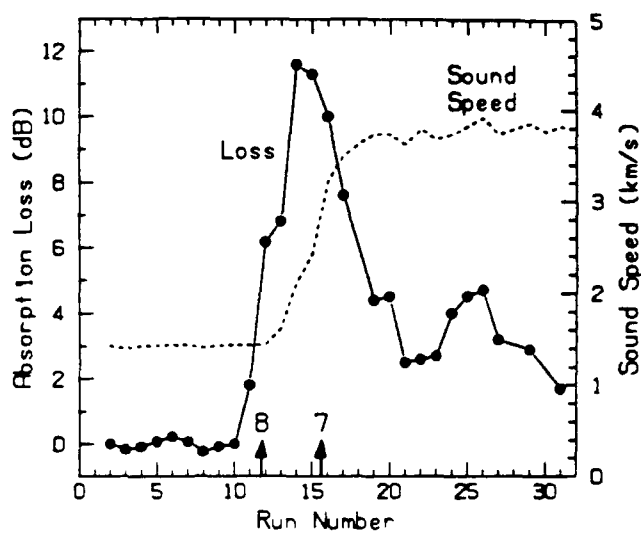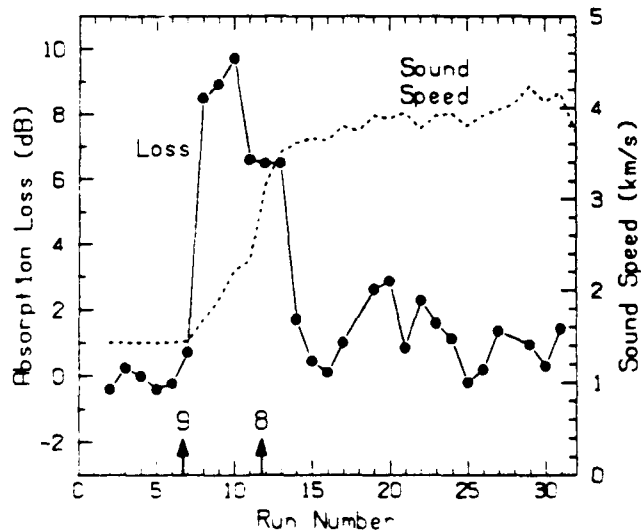
FIG. 11. Signal loss and sound speed in the interval between hydrophones pairs: (a) 7–8 and (b) 8–9. The arrows indicate when each hydrophone was frozen into the ice. When a hydrophone pair is sampling the skeletal layer, the loss is large—perhaps excessive—since it includes effects due to sensitivity change. As the ice advances, the hydrophones are left in solid ice which has a low absorption. The sound speed gradually increases as more and more of the interval becomes ice.

A best-fit second order curve for the data shows, by its intercept, a boundary transmission loss of 4.5 dB. Since the speed is faster in the ice, implying that the pressure transmission coefficient should be greater than 1 (assuming no density change), this loss must be primarily an artifact of reduced hydrophone sensitivity. The slope of the curve near $qs=0$ gives a peak loss rate of ~~1.9~~ *1.8* dB/cm, an upper limit to the skeletal layer absorption coefficient. ~~Figure 12~~ *The second order curve* shows a total absorption in the 0-3 cm skeletal layer of 4 dB, *which* is a little higher than the 2.3 dB quoted above from previous work. A fourth degree curve has been added (dotted line) to provide a better fit in the skeletal layer. This curve indicates a peak loss of ~~about 5~~ dB/cm *rate. 4.4* in the skeletal layer *and a total absorption*. A statistical F-test of the data in Fig. 12 indicates that the decrease in X^2 using the second-order fit (as compared to a linear fit) is significant at the 94th percent level. For the fourth-order fit, the decrease is significant at the 90th percent level.

The slope of the curve at any point also determines the value of the coefficient k mentioned above, which goes from 1.0 (2.5 for the fourth degree curve) near the ice/water interface to 0.3. We reiterate that k would not vary if the form of the absorption throughout the ice, including the skeletal layer, was as given in Eq. (6). Taken together, our previous work[16] and the data in Figs. 11 and 12 imply a failure of this temperature dependence in the skeletal layer.

6. Reflections from the underside of ice

Interleaved between the 92 kHz transmission measurements from the platter transducer to the hydrophones were measurements of the return to the platter from the underice surface at several frequencies. A comparison with initial water surface returns gave an amplitude reflection coefficient.

Coefficients were calculated for each set of measurements. Because of rather high variability, an average was taken for the several runs of each day. These are plotted in Fig. 13. The 220 kHz values were too variable and have been omitted (the beam is very narrow at 220 kHz, and the spot size may have been too small to provide adequate averaging).

Figure 14a gives averages of the reflection coefficients measured during freezing, along with results from earlier measurements for the undersurface of the canopy. The coefficients, and the de-
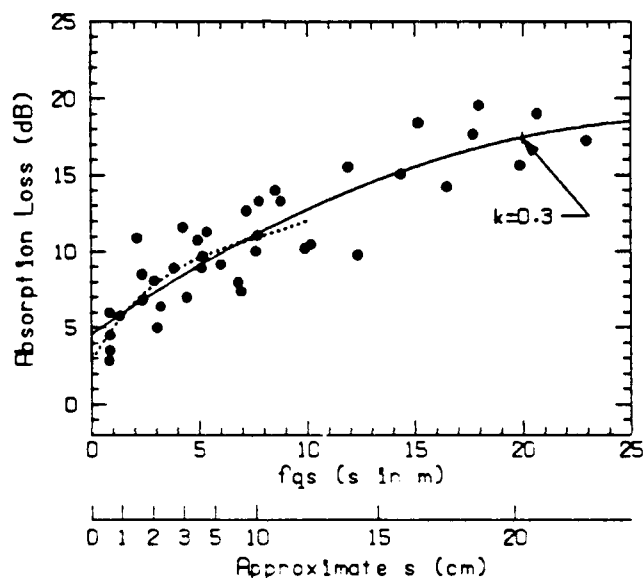
14

FIG. 12. Signal loss measured between hydrophones and calculated for various distances s into the ice. The loss is plotted versus the integral of *fqs*, where *f* is the frequency and *q* includes the temperature dependence of the absorption. The slope in this plot is the absorption constant *k* in Eq. (6). A second degree best fit curve shows that *k* is high in the skeletal layer and then drops off farther into the ice. A fourth degree curve (dotted) gives a better fit for the 3-cm skeletal layer.
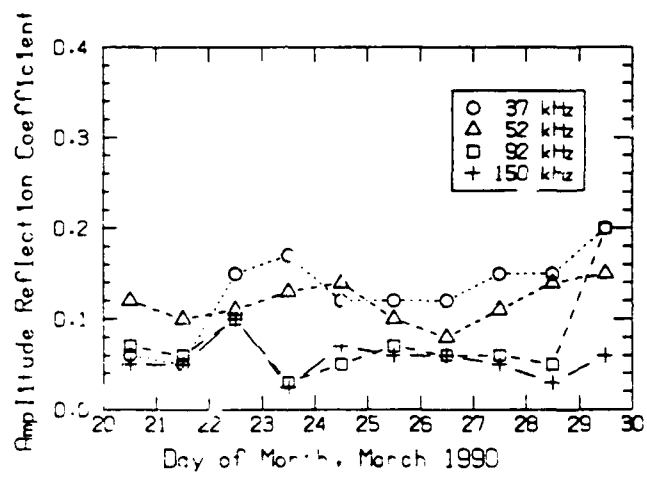
FIG. 13. Daily averages of the amplitude reflection coefficients at several frequencies obtained during ice growth

crease with frequency, agree well. Also shown is the theoretical prediction of the reflection coefficient (labeled ★) using the sound speed profile

theory

$$c(s) = \begin{cases} c_1 & s < s_0 \\ c_4 + (c_3 - c_4)\{1 - \tanh[\delta_0(s - s_0)]\} + \frac{1}{2}(c_2 - c_4)\{1 + \tanh[\delta_i(s - s_i)]\} & s > s_0 \end{cases} \tag{9}$$

with

$$s_0 = 0.0 \text{ m}, \quad s_i = 0.065 \text{ m}, \quad c_1 = 1436 \text{ m/s}, \quad c_2 = 4000 \text{ m/s}, \quad c_3 = 1490 \text{ m/s},$$

$$c_4 = 3600 \text{ m/s}, \quad \delta_0(c_4 - c_3) = 90{,}000 \text{ (s}^{-1}\text{)}, \quad \frac{1}{2}\delta_i(c_2 - c_4) = 1100 \text{ (s}^{-1}\text{)}.$$

and a density of 0.959 g/cm^3. Equation (9) is plotted in Fig. 14b, with the curve from Fig. 10c shown as a dotted line for comparison. Here, c_1 is sound speed in water, c_2 is bulk sound speed in the interior of the ice, c_3 is sound speed in the ice at the ice/water interface, and c_4 is sound speed at one point between s_0 and s_i. The theoretical calculation[17] is discussed in Section IV of Ref. 8 where it was used to predict the sound speed profile in the ice using the reflection coefficient data for 1988 shown in Fig. 14. The skeletal layer was predicted to be 2 to 3 cm thick (Fig. 16a of Ref. 8). The comparison shown here between reflection data and theoretical calculation using a known sound speed profile demonstrates the utility of the type of acoustic inversion performed in Ref. 8.

B. Submerged Ice Block

1. Ice block appearance

The second phase of the experiment was initiated by coring out a 58-cm diameter cylindrical block, centered on the sensor arrays, using an APL thermal drill.[18] The block was then held down with a rigid structure. An underwater videotape of the block, taken after the experiment was completed, clearly showed that all surfaces of the block were fuzzy due to ice growth. Efforts to reproduce the view for this article resulted in Fig. 15, in which everything looks fuzzy. Above the block is the tripod structure; the ends of the sensor arrays are visible at the bottom of the block.
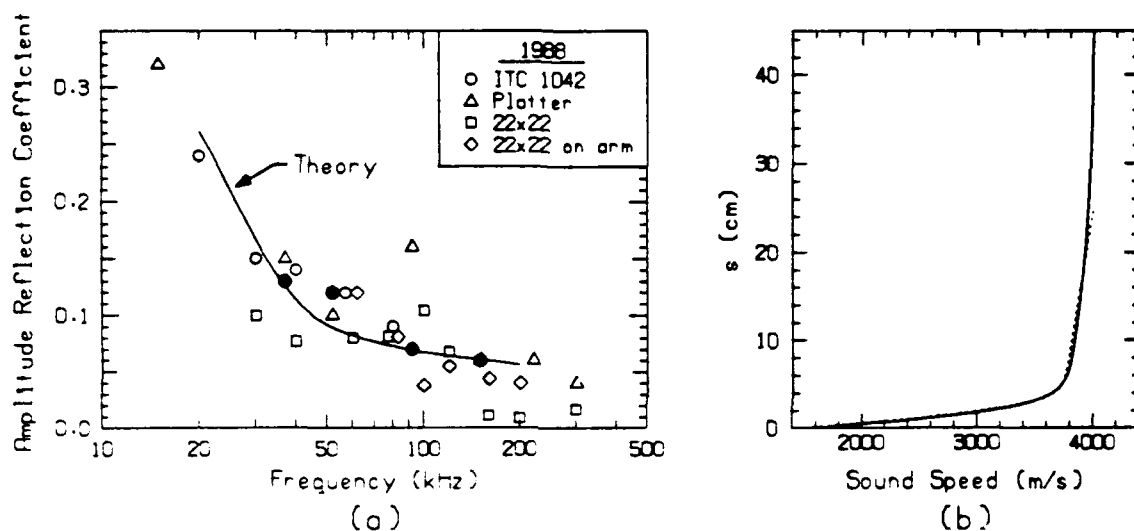
FIG. 14. In (a), the average amplitude reflection coefficients for all measurements during ice growth (filled circles) are compared with ice canopy reflectivities measured in 1988. In (b), the dotted line is the sound speed profile derived from measurements (the heavy curve of Fig. 10c). The solid line in (b) was calculated using Eq. (9) with parameters selected to obtain a good representation of the data; it was used to predict the curve in (a).

FIG. 15. An underwater view of the submerged ice block.

2. Temperature monitoring and calculation of thermal diffusivity

The readings of temperature in the ice block were continued after it was submerged. The profiles obtained are plotted in Fig.16. On the last set of readings the entire block was near the temperature of the water. We used profiles taken 0.4, 8, and 16 hours after submergence (run numbers 1, 17, and 19) to calculate an "effective" thermal diffusivity (see appendix), assuming no spatial or temporal variance in the block's thermal diffusivity. The value obtained is between 0.0013 and 0.0018 cm^2/s, about one-fifth the value calculated earlier.

A two-dimensional array of thermistors would allow a more complete calculation of the diffusivity, taking into account the temporal variability of the thermal diffusivity within the block. However, one can qualitatively explain the low value of effective diffusivity in the submerged block by examining the equation given for the dependence of diffusivity on salinity, temperature, and density [Eq. (A16) in the appendix] and using an electrical analogy.[19] For the present temperatures (-10°C to -1.8°C) the term in brackets in the denominator (the specific heat) varies most dramatically. It is about ten times larger in the outer portion of the ice, implying a much lower diffusivity there. Using the electrical analogy of Ref. 19 and treating the block in layers, one finds that the capacitance of the outer portion of the block is in parallel with the inner portion, and the time rate of change of the temperature is dominated by the high capacitance region. Physically, the outer portion of the block can absorb a large amount of heat via phase changes (latent heat is part of the specific heat given here) with a small change in temperature. This tends to shield the inner portion. Thus the temperature change there is small. More formally, the high capacitance in the outer portion affects the inner portion temperature change due to the "boundary" conditions of continuity of temperature and heat conduction between the inner and outer portions of the ice.

3. Sound speed monitoring

The submergence phase of the experiment was divided into seven time periods. For each, a sound speed was computed in each hydrophone interval by averaging the data obtained in that period. The results are plotted in Fig. 17. At most depths there was a rapid change in sound speed followed by a slow drift as the block was warmed by the water. The sound speeds for the deepest
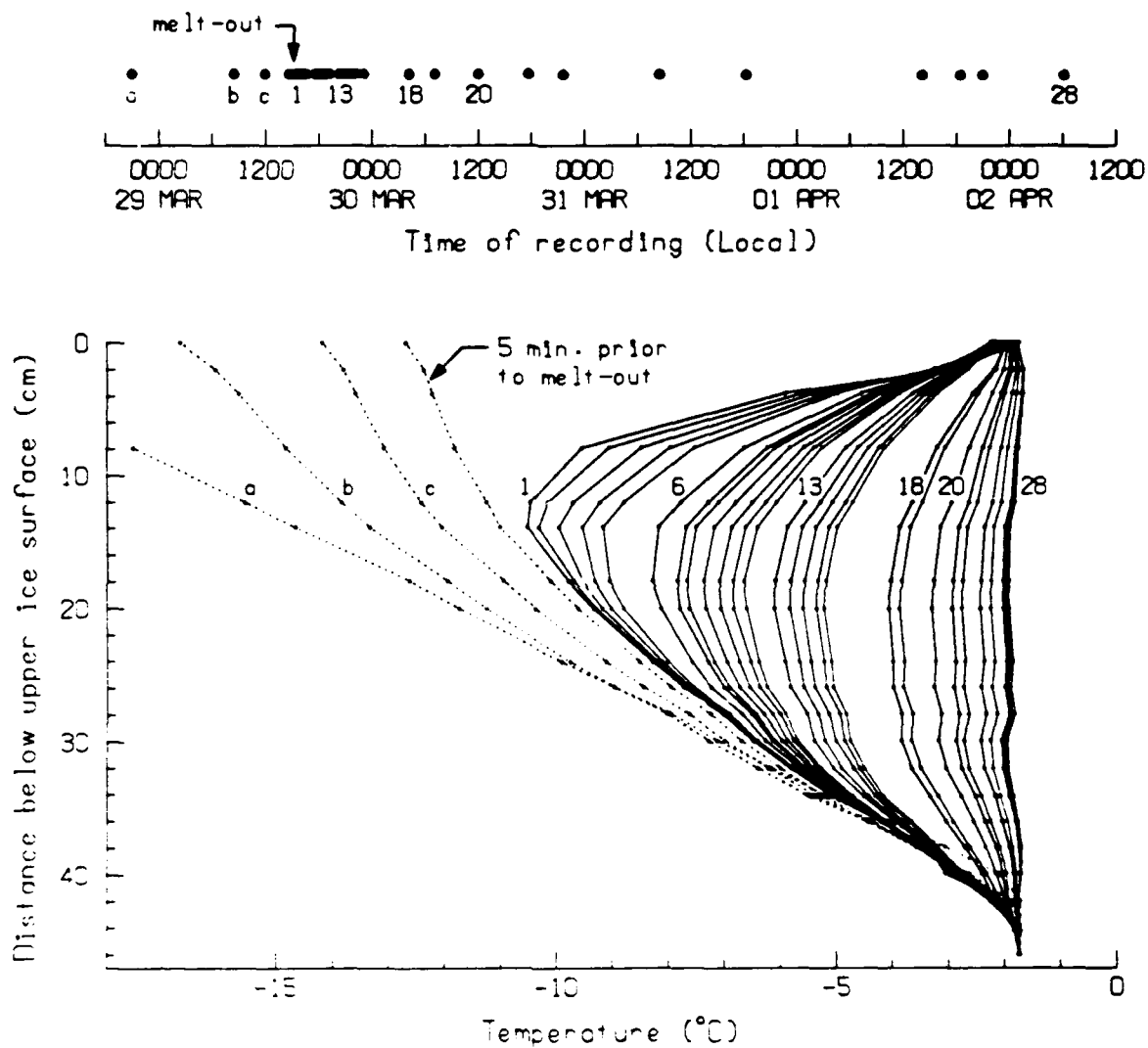
FIG. 16. Temperature profiles in the submerged ice block during the four days it took for the block to warm to the temperature of the water. The four profiles taken before coring are the same four shown as dotted in Fig. 8. As in Fig. 8, several profiles are labeled by run number, and the graph at the top of the figure associates run number with local time.

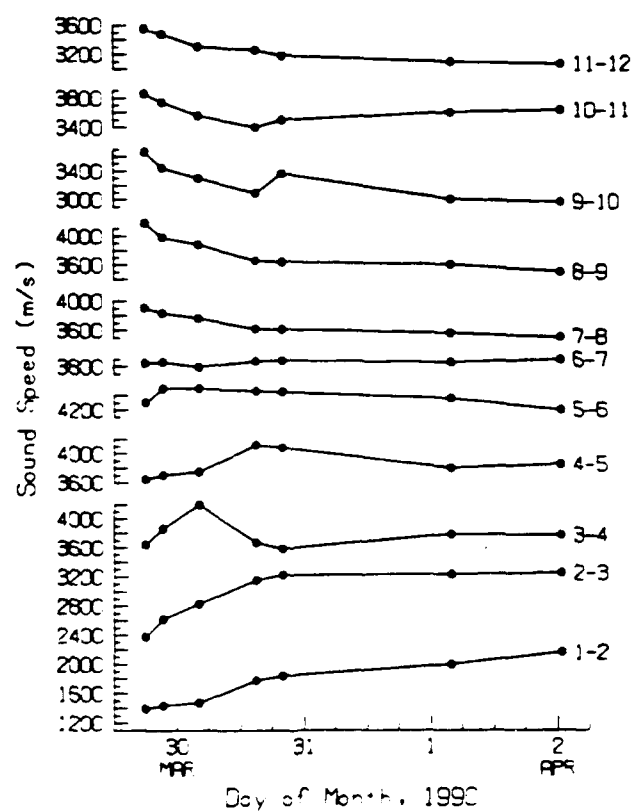FIG 17. Sound speed between hydrophone pairs. obtained by averaging over successive time intervals. The first measurement took place 2 hours and 20 min after the block was submerged.

hydrophone interval increase with time because additional ice formed in the interval after submergence owing to heat conduction into the ice above. At the upper levels the sound speed decreases as the ice warms. For hydrophone pairs 3-4, 4-5, and 5-6 the speed goes through maxima after submergence.

An alternate view of the hydrophone data is shown in Fig. 18. Here sound speed profiles in the ice before submergence and for several time intervals after submergence are derived from the data. Note that the sound speed maxima for the first day in hydrophone pairs 3-4, 4-5, and 5-6 are also associated with a maximum in the sound speed profile. Indeed, one sees that from the bottom of the block until at least 15 cm above this interface there is an increase of speed with time during part of the experiment, the greatest increase occurring about 11 cm from the bottom. The data again indicate that some short time scale effect causes the profile to have a maximum which then relaxes via a much longer time scale mechanism.

The long time scale relaxation of the profile can be attributed to warming of the block. The short time scale effect was unexpected. At present we believe it can be explained by disruption of the hydrostatic equilibrium when the block is pushed down into the water. To support this hypothesis, we first recall the analysis of Eide and Martin,[14] who have calculated the pressure within a brine drainage channel and the hydrostatic pressure at a height z above the ice/water interface to explain the expulsion of brine in young growing sea ice. Using their Eq. 7a and b, the volume flux (Q) out of a model brine drainage channel of constant radius (r) is

$$Q = \frac{\pi r^4}{8 \rho_b v_b H_2} (p_b - p)$$
(10)

where ρ_b is the mean density of the brine in the channel, v_b is the mean viscosity of the brine, H_2 is the level of the brine in the channel, p_b is the brine hydrostatic pressure at the bottom of the channel, and p is the seawater hydrostatic pressure at the bottom of the channel. During the freezing process, gravity drainage of the heavier brine to obtain pressure equilibrium at the lower surface of the ice results in voids in the upper part of the drainage channels. In submerging the block
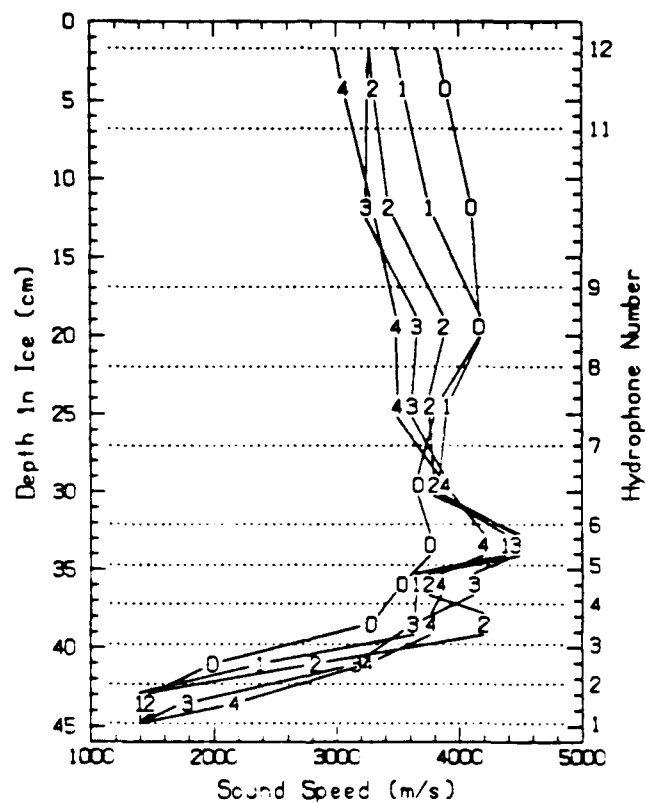
FIG. 18. Sound speed measurements for the submerged phase. The profile labeled 0 is the last one taken before coring of the block; profile 1 is the average of four measurements 5 h after submergence; 2 is after 12 h of warming; 3 is after 1 day's warming; and 4 was taken after 4 days of warming.

such that the top is at 1 m depth, we have increased p in Eq. (10) by about 10^4 N/m^2 (1.5 lb/in^2). With the assumption that the upper surface of the ice is impermeable compared with the lower part of the ice, this results in a flux of low salinity sea water into the brine channel, lowering the salinity of the brine. Because this lower salinity brine is now out of thermal equilibrium, freezing occurs and brings the brine salinity up to its equilibrium value.[7] The hypothesis is that this effect produces the increase in speed seen in the bottom part of the ice, in a manner to be discussed below. If this is the correct explanation, the region near the lower water/ice interface (15 cm thick) that experiences an increase in sound speed may be the region where brine drainage channels occupy a significant volume of the bulk ice. That distance is about one-third of the ice thickness in this case.

Porosity is one of the major parameters determining the speed of sound in ice.[8,11] One mechanism by which a maximum could be developed in the vertical profile is, therefore, if the salinity reduction by seawater influx was sufficient to reduce the porosity by the necessary amount. At the end of the submergence phase we took an ice core and measured the salinity profile. Figure 19 shows the profiles obtained then and at the end of the ice growth phase. These profiles and the appropriate temperature profiles were used to obtain the porosity profiles shown in the figure. Also displayed is sound speed profile No. 4 from Fig. 18. The lower salinity near the peak in sound speed at 30 cm depth qualitatively confirms the physical picture given above. However, the effect on porosity is not sufficient to predict the speed enhancement using present model parameters. To demonstrate this, in Fig. 20 we compare the experimental results with the results using the porosities of Fig. 19 in two different models of porosity vs sound speed.[8,11] Figure 20a shows model vs experiment at the end of the ice growth phase; Fig. 20b shows model vs experiment at the end of the submergence phase. Only a slight increase is seen in the model results for the area of reduced salinity; a large increase is observed in the experimental results.

The porous model of ice in Ref. 11 suggests another mechanism for the increase in speed. One of the parameters in that model, in addition to porosity, is the bulk modulus of the solid ice frame. If the freezing process causes a more rigid frame structure, the acoustic speed increases. Since the freezing that would occur via the influx of salt water upon submergence is certainly not the typical
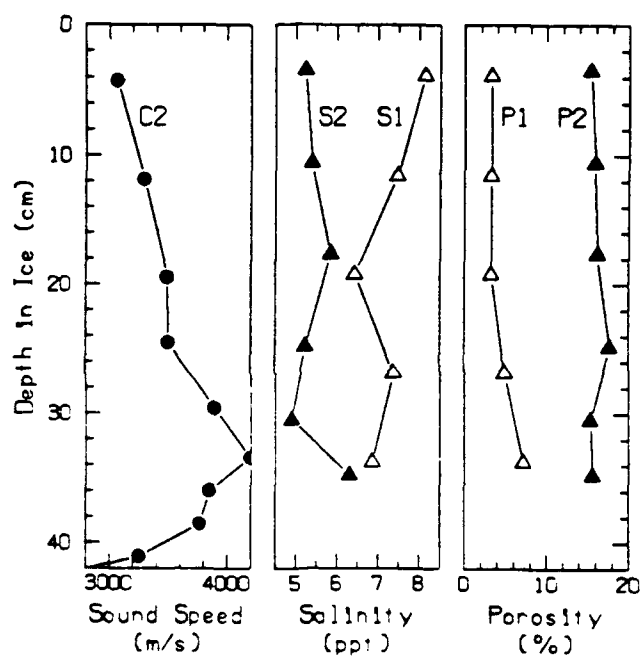
FIG. 19. Measured salinities of the ice cores before submergence (S1) and after warming (S2) were used to calculate porosity. The sound speed profile from Fig. 18 (No. 4) is plotted to show how the peak at 32 cm corresponds to a low salinity.
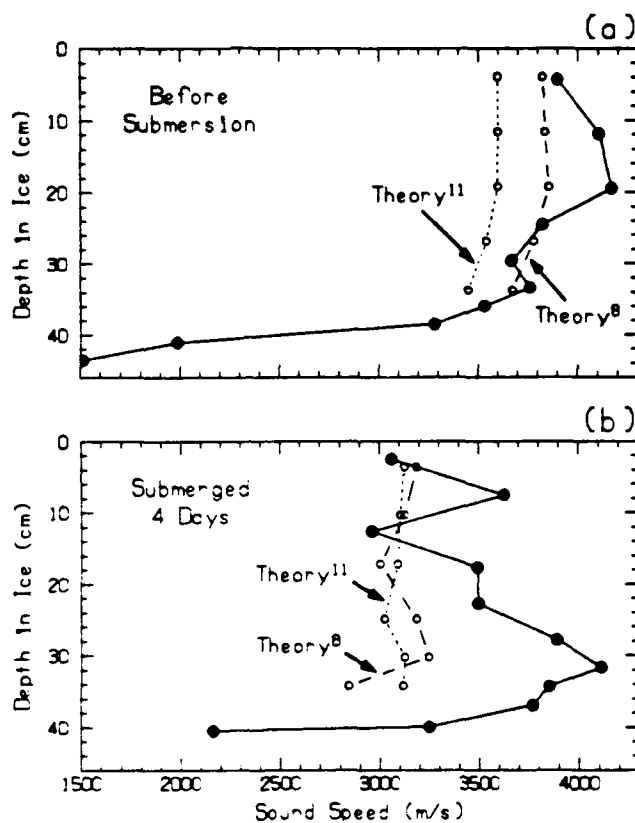
FIG. 20. Measured sound speed profiles (a) before and (b) after 4-day submersion are compared with those calculated from measured temperature and salinity profiles in ice cores using the models in Ref. 8 (dashed line) and Ref. 11 (dotted line). Note that the reduced salinity seen in Fig. 19 is not sufficient to produce the high sound speed seen near the bottom of the ice after submersion for 4 days.

freezing process in ice growth, it is possible that the frame rigidity is different. There is some previous evidence of variations in speed not related to porosity. In Ref. 20 a different Young's moduli versus porosity curve was found for winter ice than for summer ice. The authors commented that the Young's modulus might also depend on temperature. Within the porous ice model this is equivalent to saying the frame rigidity depends on temperature, a contention that seems reasonable.

4. Absorption changes

As in the ice growth phase of the experiment, sound pulses transmitted into the block from below were also used to determine absorption. For each ping we compared the amplitudes at two adjacent hydrophones. The ratio was compared with the in-water ratio obtained for these two hydrophones before the ice began to freeze.

Temperatures were measured every few hours. There were twice as many thermistors as hydrophones, so the temperature gradient between hydrophones was well known. We calculated the absorption loss from the amplitude ratio as in Eq. (4). For each run, a plot of cumulative absorption loss vs cumulative qs for hydrophones 1-9 gave eight points. A best fit line gave a slope equal to k. The average k was (0.3 ± 0.1). This is 60% higher than our 1988 results,[16] but in good agreement with that shown in Fig. 12. The variation of k during the 5 days of submergence is shown in Fig. 21. Individual k's are erratic. There is no appreciable trend in k with time, which suggests that the temperature dependence given by McCammon and McDaniel [Eq. (6)] is appropriate. This test is a moderately good one because the $T^{-2/3}$ dependence gives a doubling of the absorption for the 5-day temperature change from an average of -6°C to -2°C.

5. Underice reflectivity changes

After the block was cored out and depressed, readings of the return from the lower surface of the block were obtained to monitor the effect of block warming on the amplitude of the reflection coefficient. The return from the block was converted to target strength and then compared with the theoretical target strength of a 58-cm diameter rigid plate. The difference is $20 \log Ra$, where Ra is the amplitude reflection coefficient. It is computed and plotted in Fig. 22, which shows a decrease

FIG. 21. Measurements of absorption coefficient k during the 4 days of block submersion. A least squares line shows only a small slope, supporting the temperature dependence of Eq. (6).

FIG. 22. Measured amplitude reflection coefficients during the warming phase. Although the scatter of individual measurements was large. averages for each day show a decreasing trend after the initial increase when the block is submerged.

in Ra as the block warms. Figure 23a gives the reflection coefficient as a function of frequency at the end of the experiment, compared again with the 1988 results and experimental results in Fig. 14a. Also shown is a theoretical prediction calculated using Eq. (9) but with

$$s_0 = 0.0 \text{ m}, \quad s_t = 0.16 \text{ m}, \quad c_1 = 1436 \text{ m/s}, \quad c_2 = 3300 \text{ m/s}, \quad c_3 = 1500 \text{ m/s},$$

$$c_4 = 4400 \text{ m/s}, \quad \delta_0 (c_4 - c_3) = 50,000 \ (1/s), \quad 1/2 \ \delta_t (c_2 - c_4) = -15000 \ (1/s).$$

Equation (9) with the parameters above is plotted in Fig. 23b and compared with the experimental profile shown in Fig. 20b. Again, data and theory agree well; both show a decrease due to the relaxation of the speed gradient at the bottom of the ice.

III. SUMMARY

We have presented an overview of some of the in-situ ice properties of growing and newly submerged sea ice. Together, the ice growth and subsequent block submergence approximate the life cycle of an individual block in a newly formed ice keel.

One of the main motivations of this work was to examine the acoustic properties of highly porous regions of ice. In this regard, the high resolution sound speed profiles shown in Figs. 10 and 18 are of primary importance. Such in-situ results are needed for predicting acoustic scattering from the arctic canopy--a specific example is the prediction of normal incidence reflectivity as shown in Figs. 14 and 23. The results for the growing ice (Fig. 10) show an acoustic skeletal layer (defined as having an acoustic speed of ≤ 3500 m/s) with a thickness of about 3 cm. The concurrent measurement of scattering from the growing ice, to determine reflection coefficients, demonstrated the viability of sensing remotely from below to determine the longitudinal wave acoustic speed of the sea ice. The frequency dependence of the reflection coefficient measured during the ice growth phase agrees with previous work, and the sound speed profiles inferred from that work are very close to the ones shown here (Fig. 10).

Absorption was also measured in situ. The data show peak values in the skeletal layer between 2 and 5 dB/cm at 92 kHz. Using the temperature dependence of the McCammon-McDaniel equation [Eq. (6)], the constant k decreases from a high, poorly defined value (1-3) at the interface to, for example, a value of 0.3 at 20 cm into the ice. In the submerged ice block, a k of 0.3 was deter-
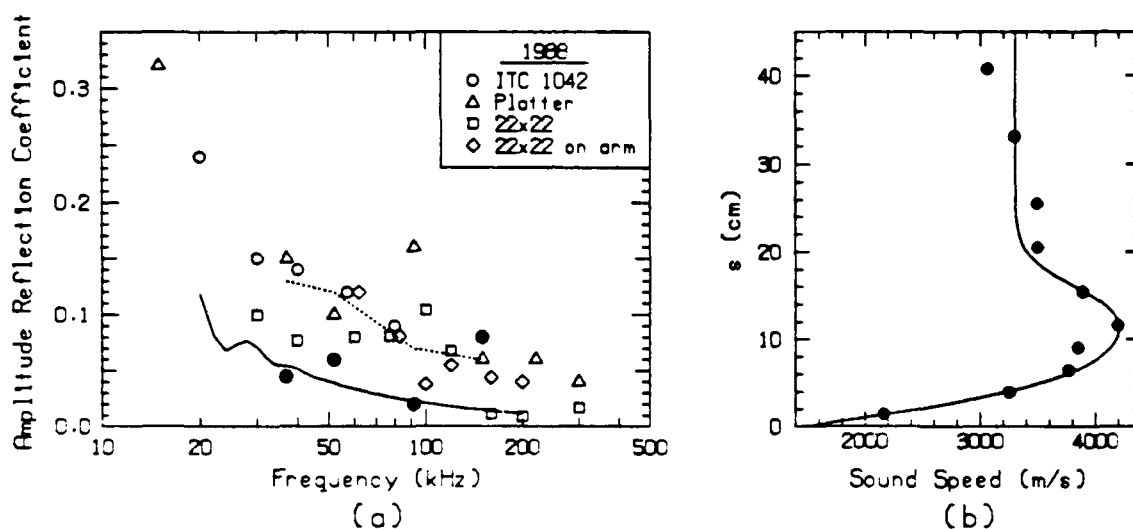
FIG. 23. In (a), the average amplitude reflection coefficients for all measurements during the submerged phase (filled circles) are compared with ice canopy reflectivities measured in 1988. The dotted line represents the data from Fig. 14 for the ice-growth phase. In (b), the sound speed data for the end of the submerged phase is a re-plot of sound speeds shown by the #4 curve in Fig. 18. The line is a fit of Eq. (9) to the data, and this profile was used to predict the solid line in (a).

mined as the block warmed to the water temperature, thus providing a check on the temperature dependence seen in Eq. (6). The scatter of the data for k during this period (Fig. 21) is large but no noticeable trend is seen. This indicates that the temperature dependence, which is a result of assuming that intergra .ı interaction controls the absorption, is useful in this case. This implies that, though the porosity increases, a pore structure remains which prevents other effects (such as fluid viscosity in the Biot model) from altering the temperature dependence of the absorption.

The measured temperature profiles in the ice were used to calculate the thermal diffusivity in the upper portion of growing ice (0.0080 cm^2/s) and in the submerged ice block (about 0.0015 cm^2/s). The difference between these values was related to the change of specific heat of the ice as a function of temperature. Measured salinity and temperature profiles allowed calculation of porosities in the growing and submerged ice. These porosities were then used in two models. Figure 20a shows comparisons between model and experiment during ice growth. The subsequent comparison to the experimental profile in the submerged block (Fig. 20b) suggests that porosity changes alone are not responsible for the high speed regime seen there.

Sound speed profiles taken during the submergence portion of the experiment (Fig. 18) show effects from long (up to 80 hours) and short (a few hours) time scale processes. The long time scale effect corresponds to the time scale of block warming. The short time scale process is hypothesized to be the result of disruption of the hydrostatic equilibrium by block submergence. We believe the submergence forces seawater into the block, thereby reducing the salinity in brine drainage channels within the bottom third of the ice, which reduces the porosity through freezing and also changes the ice frame rigidity. A reduced salinity in the region of increased sound speed supports this hypothesis. Additional information regarding this work is given in Ref. 23.

ACKNOWLEDGMENTS

esis for the short time scale speed change in the bottom one-third of the ice after submergence.

REFERENCES

1. C. H. Yew and X. Weng, "A study of reflection and refraction of waves at the interface of water and porous sea ice," J. Acoust. Soc. Am. **82**, 342-353 (1987).

2. G. C. Bishop, W. T. Ellison, and L. E. Mellberg, "A simulation model for high frequency under-ice reverberation," J. Acoust. Soc. Am. **82**, 275-286 (1987).

3. D. A. McCammon and S. T. McDaniel, "The influence of the physical properties of ice on reflectivity," J. Acoust. Soc. Am. **77**, 499-507 (1985).

4. B. E. Miller and H. Schmidt, "Observation and inversion of seismo-acoustic waves in a complex arctic ice environment," J. Acoust. Soc. Am. **89**, 1668-1685 (1989).

5. H. E. Huppert and M. G. Worster, "Dynamic solidification of a binary melt," Nature **314**, 703-707 (1985).

6. J. S. Wettlaufer, "Directional Solidification of Salt Water: Deep and Shallow Cells," submitted to *Europhysics Letters.*

7. G.F.N. Cox and W. F. Weeks, "Equations for determining the gas and brine volumes in sea ice samples," CRREL Report 82-30 (1982).

8. G. R. Garrison, R. E. Francois, and T. Wen, "Acoustic reflections from arctic ice at 15-300 kHz," J. Acoust. Soc. Am. **90**, 973-984 (1991).

9. T. Wen, G. R. Garrison, and R. E. Francois, "Melt season changes in arctic ice," IEEE Oceans'80 Conference Proceedings, 114-122 (1980).

10. R. Stein, "A modular acoustic measurement system," Proceedings IEEE Oceans'83, 176-181 (1983).

11. K. L. Williams and R. E. Francois, "Sea ice elastic moduli: Determination of Biot parameters using in-field velocity measurements," J. Acoust. Soc. Am. (in press, 1992).

12. G. A. Maykut, "An introduction to ice in the polar oceans," Applied Physics Laboratory Report APL-UW 8510 (1985).

13. G.F.N. Cox and W.F. Weeks, "Brine drainage and salt entrapment in sodium chloride ice."

CRREL Research Report 345 (Dec. 1975).

14. L. I. Eide and S. Martin, "The formation of brine drainage features in young sea ice," J. Glaciol. **14**, 137-154 (1975).

15. R.D. Stoll, "Waves in saturated sediments," in *Physics of Sound in Marine Sediments*, edited by L. Hampton (Plenum Press, New York, 1974).

16. T. Wen, G. R. Garrison, R. E. Francois, R. P. Stein, and W. J. Felton, "Sound speed, reflectivity, and absorption measurements in arctic ice in 1988," Applied Physics Laboratory Report APL-UW TR 9005 (1991).

17. D. P. Winebrenner, "Acoustic backscattering from sea ice at high frequencies," Applied Physics Laboratory Report APL-UW TR 9017 (in preparation).

18. R. E. Francois and J. G. Harrison, "A thermal drill for making large holes in sea ice," IEEE Oceans '75 Record, IEEE Pub. 75CH0995-1 OEC, 303–310 (1975).

19. V. Paschkis and H. D. Baker, "A method for determining unsteady-state heat transfer by means of an electrical analogy," Trans. Am. Soc. Mech. Eng. **64**, 105–112 (1942).

20. M. P. Langleben and E. R. Pounder, "Elastic parameters of sea ice," in *Ice and Snow*, edited by W. D. Kingery, (MIT Press, 1963) pp. 69-78.

21. A. L. Fetter and J. D. Walecka, *Theoretical Mechanics of Particles and Continua* (McGraw-Hill, New York, 1980) p. 417.

22. G. E. Roberts and H. Kaufman, *Table of Laplace Transforms* (W. B. Saunders, Philadelphia, 1966).

23. K. L. Williams, P. D. Mourad, R. E. Francois, T. Wen, G. R. Garrison, and W. J. Felton, "Sound speed, reflectivity, and absorption measurements in arctic ice in 1990," Applied Physics Laboratory Report APL-UW 9208 (in preparation).

APPENDIX - Calculations of Thermal Diffusivity

During Ice Growth

We use the warming trend seen in Fig. 4 (29 March) and the resulting change in temperature profile shown in Fig. 8 to estimate the thermal diffusivity of the ice. To begin, a vertical coordinate (z) is established with origin at the ice/water interface and positive direction upward toward the ice/air interface. With this coordinate system, a known ice thickness of 42 cm, and the thermistor readings at the ice/air and ice/water interfaces, the following initial and boundary conditions were established:

$$T(z, 0) = -1.8°C - (0.5 \frac{°C}{cm})z, \qquad (A1)$$

$$T(0, t) = -1.8°C, \qquad (A2)$$

and

$$T(42cm, t) = -22.8°C + (1.54 \times 10^{-4} \frac{°C}{second})t. \qquad (A3)$$

Equation (A1) is a linear approximation of the temperature profile at the beginning of the warming trend. Equation (A2) is the approximate water/ice interface temperature. Equation (A3) is a linear approximation to the time dependence of the upper thermistor during the warming trend.

After rewriting these conditions using the variable $T = T + 1.8$, we solve the homogeneous equation of heat conduction

$$\frac{\partial^2 T}{\partial z^2} = \frac{1}{\kappa}\frac{\partial T}{\partial t} \qquad (A4)$$

with the conditions

$$\bar{T}(z,0) = -0.5z \quad , \tag{A5}$$

$$\bar{T}(0,t) = 0 \quad , \tag{A6}$$

and

$$\bar{T}(42,t) = -21.0 + (1.54 \times 10^{-4})t \quad . \tag{A7}$$

In Eq. (A4) the parameter κ is the thermal diffusivity whose numerical value we shall predict.

Next, Eq. (A4) is Laplace transformed giving (Ref. 21, p. 420)

$$\frac{d^2}{dz^2}\bar{T}(z,s) - \frac{s}{\kappa}\bar{T}(z,s) = -(\frac{1}{\kappa})\bar{T}(z,t \equiv 0) \tag{A8}$$

with the transformed boundary conditions

$$\bar{T}(0,s) = 0 \quad , \tag{A9}$$

and

$$\bar{T}(42,s) = -\frac{21.0}{s} + \frac{(1.54 \times 10^{-4})}{s^2} \quad . \tag{A10}$$

Now the object is to determine $\bar{T}(z,s)$ and inverse transform to obtain $\bar{T}(z,t)$. We proceed

by finding the Green function which solves

$$\frac{d^2}{dz^2}G_s(z, z') - \frac{s}{\kappa}G_s(z, z') = -\delta(z - z') \qquad (A11)$$

with boundary conditions $G_s(0, z') = 0$, $G_s(42, z') = 0$. Standard techniques (Ref. 21, p. 247) give

$$G_s(z, z') = \frac{\sinh\left((\frac{s}{\kappa})^{1/2}z_l\right)\sinh\left((\frac{s}{\kappa})^{1/2}(z_g - 42)\right)}{(\frac{s}{\kappa})^{1/2}\sinh(-(\frac{s}{k})^{1/2}42)}, \qquad (A12)$$

where z_l is the smaller of (z, z') and z_g is the larger of (z, z').

Using the Green function defined in Eq. (A12), the solution for $\bar{T}(z, s)$ is

$$\bar{T}(z, s) = (\frac{0.5}{\kappa})\int_0^{42} z'G_s(z', z)\,dz' - \left[G_s(z', z)\frac{d}{dz}\bar{T}(z', s) - \bar{T}(z', s)\frac{d}{dz}G_s(z', z)\right]_0^{42}. \qquad (A13)$$

Substituting Eqs. (A9), (A10), and (A12) into Eq. (A13), one finds that

$$\bar{T}(z, s) = \frac{-0.5z}{s} - \left(\frac{1.54 \times 10^{-4}}{s^2}\right)\left(\frac{\sinh\left((\frac{s}{\kappa})^{1/2}z\right)}{\sinh\left((\frac{s}{\kappa})^{1/2}42\right)}\right). \qquad (A14)$$

Inverse transforming[22] Eq. (A14) and using the definition of $T(z, t)$ in terms of $\bar{T}(z, t)$ gives

$$T(z, t) = -1.8^\circ C - (0.5\frac{^\circ C}{cm})z + (1.54 \times 10^{-4}\frac{^\circ C}{second})\sum_{-\infty}^{\infty}\int_0^t erf\left(\frac{42(n + \frac{1}{2})}{(\kappa u)^{1/2}} - \frac{z}{2(\kappa u)^{1/2}} + \frac{42(n + \frac{1}{2})}{(\kappa u)^{1/2}}\right)du,$$
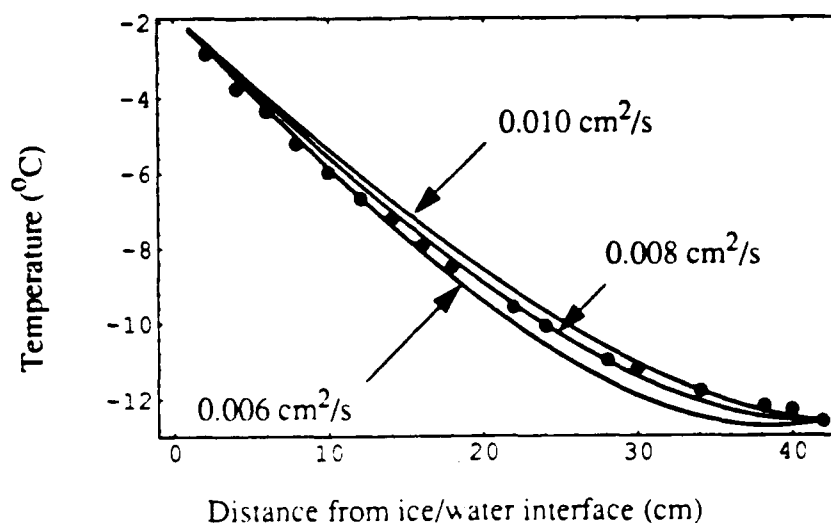
$$(A15)$$

FIG. A1. Data points for the last temperature profile taken during the ice growth phase (run 30, Fig. 8) are compared with theoretical predictions based on Eq. (A15). Predictions are shown using three different thermal diffusivities. The best visual fit is for a κ of $0.008\ cm^2/s$.

where *erf* is the generalized error function.

Equation (A15) was evaluated numerically at a time corresponding to the last temperature profile taken (run 30, Fig. 8) during the ice growth phase of the experiment. For the parameters here, including the terms $(-3)<n<3$ was adequate for convergence. Figure A1 shows the experimental temperature profile and the result of evaluating Eq. (A15) for three values of thermal diffusivity κ. The value of 0.0080 cm^2/s gives the best visual fit for temperatures less than $-6°C$.

The thermal diffusivity of the ice is in reality a function of S (salinity in ppt), T (temperature in degrees Celsius), and ρ (the density in grams per cubic centimeter). The equations in Ref. 12 give

$$\kappa = \frac{k}{\rho c_i} = \frac{(0.005 \frac{cal}{(cm)\,s\,(°C)} + (3.11 \times 10^{-4} \frac{cal}{(cm)s}) \frac{S}{T})}{\rho \left[0.505 \frac{cal}{g\,(°C)} + \left(0.0018 \frac{cal}{g\,(°C)^2} \right) T + (4.3115 \frac{cal}{g\,(°C)}) \frac{S}{T^2} \right]} \qquad (A16)$$

for temperatures above $-8°C$. In Eq. (A16), k is the thermal conductivity of the ice and c_i is its specific heat. With a salinity of about 7 ppt, a density of 0.91 g/cm^3, and a temperature of $-8°C$, Eq. (A16) predicts a diffusivity of 0.0054 cm^2/s. In contrast, pure ice has a thermal diffusivity of about[12] 0.012 cm^2/s. The value obtained experimentally here is in keeping with the limits established by these previous results.

After Submergence

Here we will use the warming of the ice block during the initial 16 hours of submergence to obtain an estimate of the thermal diffusivity. Equation (A4) is again applicable, but this time a solution of the form

$$\bar{T}(r,t) = R(r)\,S(\varphi)\,Z(z)\,e^{-\lambda t} \qquad (A17)$$

is assumed. Equation (A17) reflects the cylindrical symmetry of the submerged block; z is now defined as a down pointing vertical axis with $z=0$ at the top of the block, r is the radial coordinate with $r = 0$ at the center of the block, and φ is the azimuthal angle. The boundary conditions are

$$Z(0) = Z(z_0) = R(a) = 0 \qquad\qquad \text{(A18)}$$

where z_0 is the block thickness and a is its radius. The angular symmetry of the boundary conditions imply no φ dependence in the solution. Using Eq. (A18), a general solution to Eq. (A17) is[21]

$$\bar{T}(r, \varphi, z, t) = \sum_{n, p} \frac{(C_{n,p})}{(2\pi)^{1/2}} \left(\frac{J_0(\alpha_n \frac{r}{a})}{\frac{a}{2^{1/2}} |J_1(\alpha_n)|} \right) \left((\frac{2}{z_0})^{1/2} \sin(p\pi \frac{z}{z_0}) \right) e^{-\lambda_{n,p} t}, \quad \text{(A19)}$$

where n and p are summation indices going from 1 to infinity and

$$\lambda_{n,p} = \kappa \left[\left(\frac{\alpha_n}{a} \right)^2 + \left(\frac{p\pi}{z_0} \right)^2 \right] \qquad . \qquad\qquad \text{(A20)}$$

In Eq. (A19) the J's are Bessel functions and the parameters α_n satisfy the relation

$$J_0(\alpha_n) = 0 \qquad . \qquad\qquad \text{(A21)}$$

In Eq. (A20) κ is the thermal diffusivity.

To determine the constants $C_{n,p}$ in Eq. (A19), the initial conditions must be specified. Using the experimental data, we have $z_0 \approx 44\,\text{cm}$, $a \approx 29\,\text{cm}$ and, shortly after submergence (the first thermistor data was taken about 25 minutes after submergence), the approximate initial condition

$$\bar{T}(r, z, 0) \approx \left[(-8.7) \left(\frac{z}{11} \right) H(z) H(11 - z) - 8.7 \left(1 - \frac{(z - 11)}{(z_0 - 11)} \right) H(z - 11) H(z_0 - 11) \right] \frac{(a - r)}{a}$$

$$\text{(A22)}$$

In Eq. (A22) the H's are Heaviside functions and it is understood that at $z = 11$ cm only one term in the bracket applies. The z dependence of the initial condition was set by the vertical array thermistor data and assuming the array was located at the center of the block (it was actually a few centimeters to one side). Since we don't have a horizontal array of thermistors, the r dependence was set such that it has a linear drop from the center to the edge of the block. This r dependence is suggested both by the initial z dependence and the symmetry of the forcing function (the water surrounding the block).

Using the initial condition in Eq. (A22), the constants become

$$
\begin{aligned}
C_{np} = & \left(2\pi^{1/2}\frac{a}{\alpha_n}\right)(\frac{2}{zo})^{1/2}\left\{-(\frac{8.7}{11})\left[\left(\frac{z_0}{p\pi}\right)^2 \sin\left(\frac{11\,(p\pi)}{z_0}\right) - 11\left(\frac{z_0}{p\pi}\right)\cos\left(\frac{11\,(p\pi)}{z_0}\right)\right]\right. \\
& + 8.7(1 + \frac{11}{(z_0-11)})\left(\frac{z_0}{p\pi}\right)\left[\cos(p\pi) - \cos\left(\frac{11\,(p\pi)}{z_0}\right)\right] \\
& + (\frac{8.7}{(z_0-11)})\left[-\frac{(z_0)^2}{p\pi}\cos(p\pi) - \left(\frac{z_0}{p\pi}\right)^2 \sin\left(\frac{11\,(p\pi)}{z_0}\right) + 11\left(\frac{z_0}{p\pi}\right)\cos\left(\frac{11\,(p\pi)}{z_0}\right)\right] \right\}
\end{aligned}
$$

$$
X \quad \left[\frac{J_1(\alpha_n)}{|J_1(\alpha_n)|} - \frac{1}{((\alpha_n)^2|J_1(\alpha_n)|)}\int_0^{\alpha_n} x^2 J_0(x)\,dx\right] \quad . \tag{A23}
$$

Together, Eqs. (A19) and (A23), and the definition of T in terms of $\bar{T}$, give the solution for the spatial and time dependence of the block's temperature. These equations were implemented and the experimental temperature profiles at $t = 0$, 7.6 h, and 15.6 h used to determine an effective thermal diffusivity. Figure A2 shows the experimental data and calculations using two different diffusivities. The results indicate an effective diffusivity between 0.0013 and 0.0018 cm^2/s. A qualitative explanation for this much lower value of thermal diffusivity (compared with the result obtained in the first part of the appendix) is given in the main body of the paper.
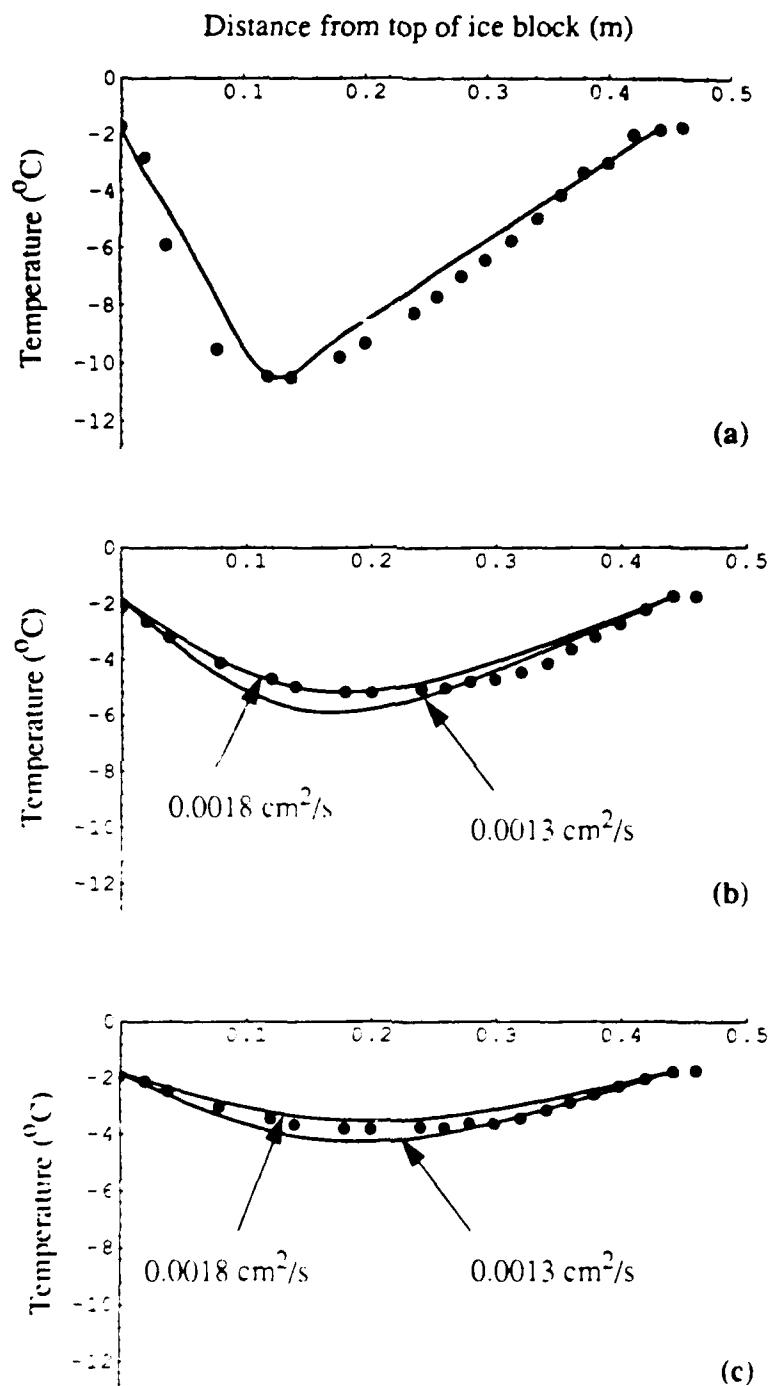
FIG. A2 The experimental temperature profiles at three times after block submergence are shown as points: (a) 25 minutes after, (b) 8 hours after, and (c) 16 hours after. Also shown are theoretical predictions based on Eq. (A19) using two thermal diffusivities.

PROJECT TITLE: Measurements of Physical Parameters and the Associated High Frequency
Backscatter of First-Year Arctic Sea Ice

INVESTIGATORS: Drs. Pierre D. Mourad and Kevin L. Williams

INSTITUTION: Applied Physics Laboratory, University of Washington

ADDRESS: 1013 N.E. 40th Street
                        Seattle, WA 98105

TELEPHONE: (206) 543-1300
OMNET: p.mourad
INTERNET: pierre@apl.washington.edu
FAX: (206) 543-6785

CONTRACT NO.:   N00014-91-J-1647

DATES: 1 January 1991 - 31 March 1992

OBJECTIVES

We aim to study independently, and to determine the relationships between: arctic sea ice acoustic wave speeds throughout the ice (especially the region near the ice/water interface); high frequency acoustic backscatter near normal incidence; and their governing physical parameters.

APPROACH

The skeletal transition zone is a primary factor in high frequency acoustic characteristics of the ice. Under the sponsorship of ONT, we designed an experiment to measure the sound speed and temperature profiles within growing and submerged sea ice while minimizing the disturbance to the skeletal transition zone. With this grant, we received the funding necessary to analyze and publish the data and its analysis as well as the underlying theory.

The experiment and the data collected during March 1990 were designed to allow examination of vertical sound speed and temperature profiles throughout the ice at a resolution not previously obtained experimentally. The experiment also allowed us to relate these profiles with both the salinity profile within the ice as well as with acoustic backscatter from the ice.

In the experiment, linear arrays (also called strings) of thermisters and transducers were suspended vertically in two large holes cut through the ice canopy down to the underlying water. We then allowed the water to freeze, capturing the instruments within the growing ice. We then made in-situ measurements of the acoustic and thermal vertical profiles within the ice. (For the former, a high frequency source below the growing ice provided the propagating wave-form received at adjacent transducers to allow calculation of the sound speed between transducer pairs.)

Immediately after each data acquisition session using the receiver string, the transmitter was placed into a transmit/receive mode to measure normal incident backscatter from the ice at several frequencies.

We extracted effective interface reflection coefficients from these data, calculated a theoretical sound speed profile within the skeletal layer to compare with the measured profile.

After the ice had refrozen to where the ice/water interface was between the deepest two receivers on the linear arrays, a cylindrical block was cut out of the ice such that the receiver and thermister strings were centered in the block. The block was submerged and, during the hours it took to come to equilibrium with the water temperature, data similar to that discussed above were acquired. This allowed monitoring of the changes in velocities and scattering properties in a block under similar conditions to blocks submerged due to ice rafting and ridging. We analyzed these data in the same way as for growing ice.

ACCOMPLISHMENTS

• Reduction of the data for compressional sound speed profiles and temperature profiles during the ice growth and submergence stages. These have high resolution in both time and in the vertical.

• Inferred bounds on and a profile of attenuation within the ice. The skeletal zone attenuates sound more efficiently than the bulk of the ice.

• Successful comparison of averages of the directly measured, high resolution compressional sound speed profiles and that inferred from measured average reflection coefficients via our theory, for growing ice (Figure 1) and submerged ice (Figure 2).

• Inferred thermal diffusivity for growing and for submerged sea ice. The former is consistent with bounds determined by measurements of diffusivity of fresh water and the calculations of G. Maykut. The latter suggests that the skeletal layer that forms across the entire surface of submerged ice acts as an insulator, decreasing the effective thermal diffusivity by reducing heat flow across the ice/water interface.

• Inferred qualitative brine-drainage channel structure within the bottom one third of growing ice based upon the response of the ice to submergence.

• Completing and will be submitting a paper on the experiment and data analysis listed above.

• Submitted paper on theory for high frequency acoustic backscatter from the rough ice/water interface of first year arctic sea ice. Results include predictions of: sound speed profiles within the skeletal layer and reflection coefficients consistent with the measurements noted above; backscatter from ice blocks, consistent with observations (Figure 3); and one dimensional (isotropic) rough-surface wave-number spectrum.

SUMMARY

We have analyzed the high-frequency acoustic properties of the ice/water interface via direct measurement of the *in situ* vertical, temporal variation of profiles of compressional sound speed, attenuation and temperature of the ice adjacent to this interface. We find that there strong gradients in the acoustic properties of this interface associated with gradients in physical properties of the ice. We have examined both the characteristics and reasons for these gradients. They affect the effective reflectivity and the acoustic backscatter from the arctic sea ice canopy. We have demonstrated a theory for backscatter and reflectivity that successfully reproduces the observations by taking into account these gradients within the ice and the roughness of the ice interface.
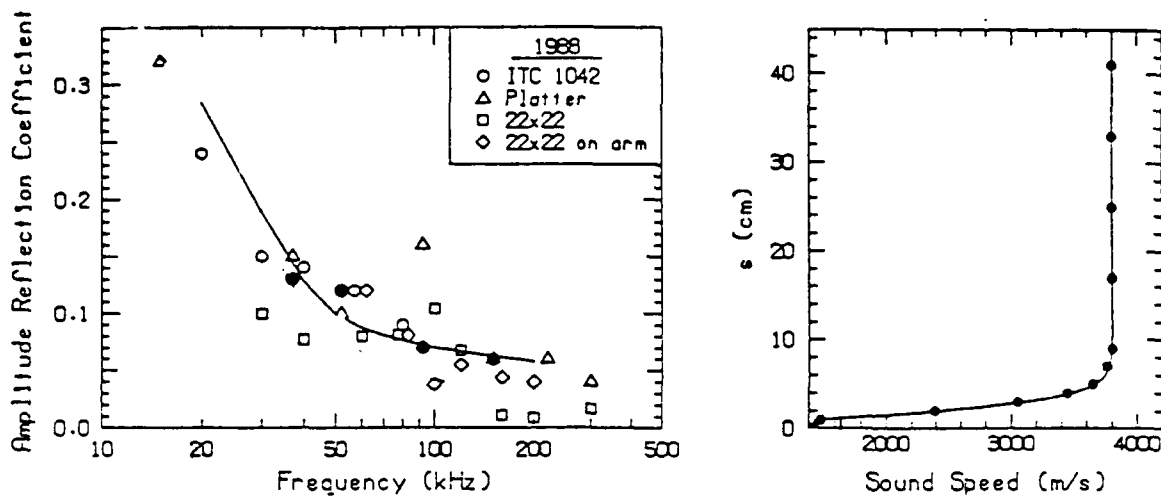
Figure 1   Comparison with theory of reflection coefficients
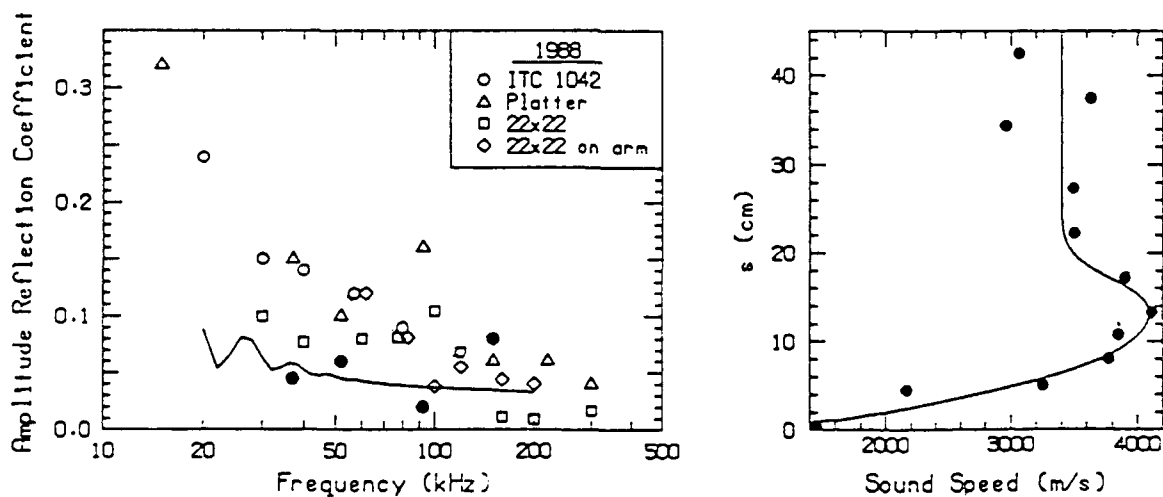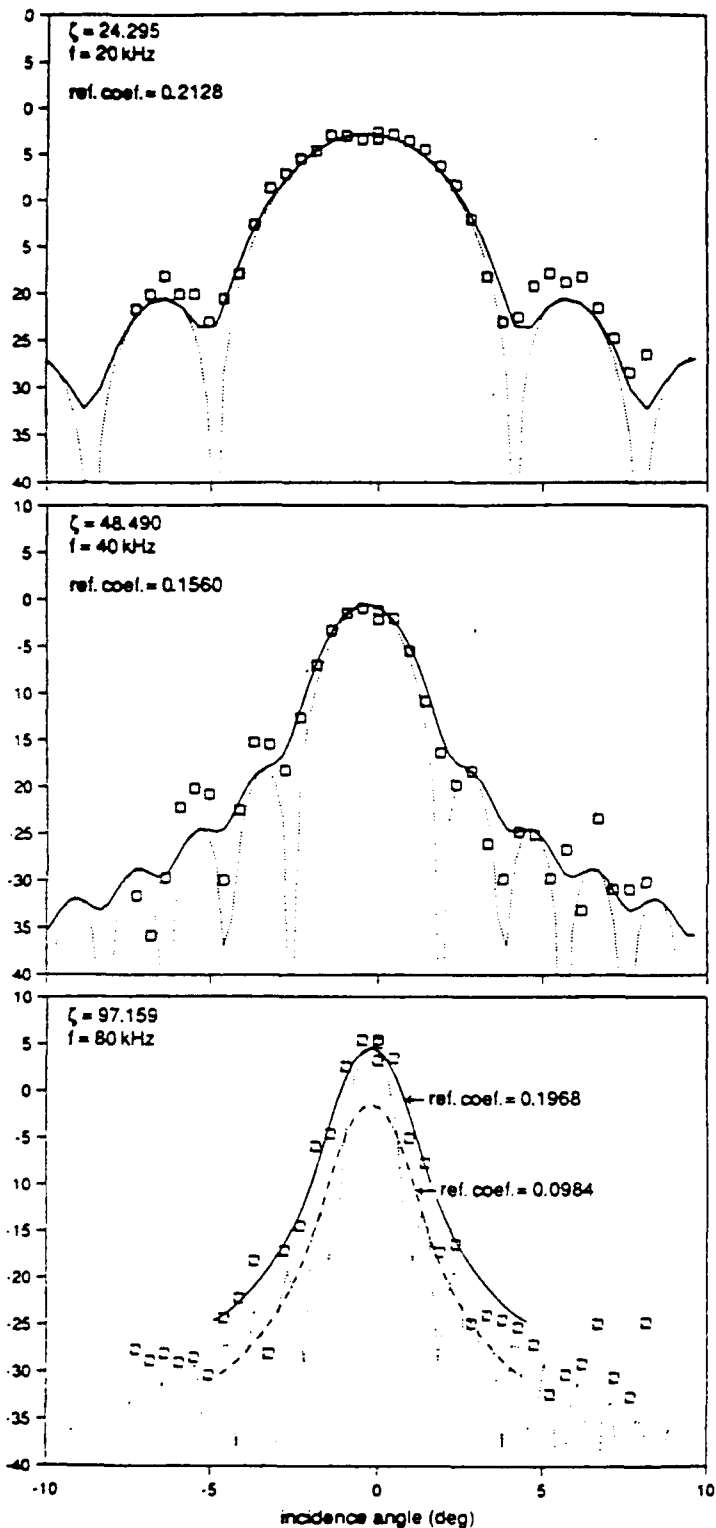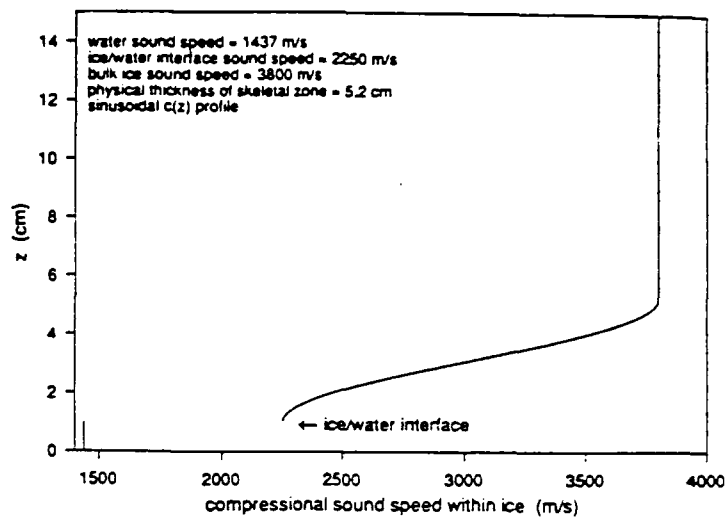measured during freezing and with those measured
for the canopy in 1988.

Figure 2 .   Comparison with theory of reflection coefficients
measured after warming and with those measured
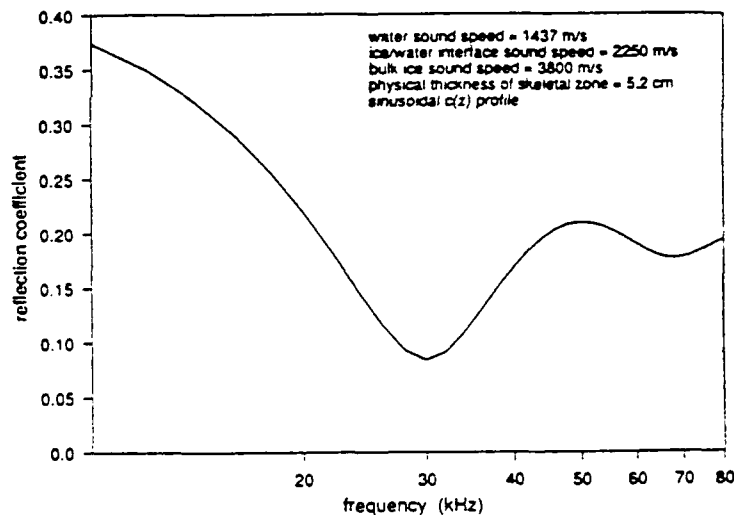for the canopy in 1988.

Figure 3. (A) Individual observed realizations of backscatter from an ice block compared with theoretical predictions of average backscatter; (B) predicted compressional sound speed profile and (C) associated frequency-dependent reflection coefficient for the ice used in (A).

PROJECT TITLE: Measurements of Physical Parameters and the Associated High Frequency Backscatter of First-Year Arctic Sea Ice

INVESTIGATORS: P. D. Mourad and K. L. Williams

Papers submitted (refereed journals)

Mourad, P. D. and K. L. Williams (1992) Near-normal incidence scattering from rough, finite surfaces: Kirchhoff theory and data comparison for arctic sea ice. Submitted to J. Acoust. Soc. Am. (attached)

Williams, K. L., G. Garrison, and P. D. Mourad (1992) Arctic sea ice: experimental examination of growing and newly submerged sea ice including acoustic probing of the skeletal layer. Accepted by
    J. Acoust. Soc. Am. (attached)